Master's thesis

NTNU
Norwegian University of Science and Technology
Faculty of Information Technology and Electrical Engineering
Department of Electric Power Engineering

Håkon Risbøl Hansen

Simulation and design of an electrodynamic Thomson coil actuator for fast mechanical switches

Master's thesis in Energy and Environmental Engineering
Supervisor: Kaveh Niayesh
Co-supervisor: Ivan Semenov
June 2022

NTNU
Kunnskap for ei betre verd

Håkon Risbøl Hansen

Simulation and design of an electrodynamic Thomson coil actuator for fast mechanical switches

Master's thesis in Energy and Environmental Engineering
Supervisor: Kaveh Niayesh
Co-supervisor: Ivan Semenov
June 2022

Norwegian University of Science and Technology
Faculty of Information Technology and Electrical Engineering
Department of Electric Power Engineering

NTNU
Norwegian University of
Science and Technology

Simulation and design of an electrodynamic Thomson coil actuator for fast mechanical switches

Håkon Risbøl Hansen

June 19, 2022

Abstract

A Thomson coil actuator is an ultra-fast electromagnetic drive mechanism to be used as the drive for the mechanical switch in a hybrid HVDC circuit breaker. Improving on the design of the TC may enable the hybrid HVDC CB to be a cost-effective CB for the protection of multi-terminal HVDC systems.

To investigate the TC mechanism, a working FEM-simulation model of the TC was made in COMSOL multiphysics. The model was verified by making a prototype and completing an experimental verification of the model. The verified model was used to complete a parametric study of the TC. The parametric study demonstrated that for any given TC, an optimized voltage to capacitance ratio of the energy source could be found. The number of turns also highly affected the efficiency and opening time, and the parametric study suggested that having a relatively high number of turns (35-45) would improve the efficiency and OT of the TC. The optimal armature radius was found to be slightly smaller than the coil radius. The change in armature thickness did not affect the eddy currents in the armature significantly (even at 4 mm) due to the poor penetration depth of the eddy currents, making the most likely limiting factor for the armature to be the force stress it experiences.

A suggestion for an iterative design process was made based on a set of generalized rules made from the parametric study. Even with the limitations set in the design process, the process became complex and intricate, highlighting the difficulty of making general dimensioning rules for such devices. The implementation of FEM-simulation models allows for faster and more cost-effective exploration of the design parameters. However, because of the many factor and parameters that affect the driving characteristics of such a device, the deriving of generalized dimensioning rules for a Thomson coil actuator has proven to be challenging.

Sammendrag

En Thomson spole aktuator er en ultra-rask elektromagnetisk driv mekanisme. Drivmekanismen skal brukes til å drive den mekaniske bryteren i en hybrid likestrøms- (HVDC) effektbryter. Ved å utbedre designet av Thomson spolen kan det muliggjøre hybrid HVDC-effektbrytere som et kostnadseffektive alternativ for beskyttelse av flerterminal HVDC-nett.

For å undersøke Thomson-spole-mekanismen nærmere ble det laget en fungerende FEM-simuleringsmodell av brytermekanismen i COMSOL multiphysics. Modellen ble verifisert ved å lage en prototype av mekanismen for deretter å bruke prototypen til å gjennomføre en eksperimentell verifisering. Den verifiserte modellen ble brukt til å gjennomføre en parameter studie av mekanismen. Paramaterstudie viste blant annet at for en vilkårlig gitt Thomson spole kan et optimalisert spenning-til-kapasitans forhold bli funnet. Det ble også vist at antall viklinger i spolen påvirket sterkt både effektiviteten og åpningstiden til mekanismen, og et relativt høyt viklingstall (35-45 viklinger) gav de beste resultatene. Den optimale armatur radiusen ble funnet til å være litt mindre en spole radiusen. Endring i armaturtykkelse hadde liten effekt, selv ved veldig tynne armaturer (4 mm), dette grunnet den dårlige penetreringsevnen til eddy-strømningene.

Et forslag til en iterativ designprosess ble laget basert på regler fra parameterstudiet. Selv med de begrensningen satt i designprosessen, ble prosessen fort kompleks og innviklet. Dette påpeker vanskeligheten ved å lage generaliserte dimensjoneringsregler for slike mekanismer. Implementeringen av FEM-simulasjonsmodeller muliggjør for en raskere og mer kostnadseffektiv utforskning av designparametere. Likevel, på grunn av de mange faktorene og parameterne som påvirker slike åpningsmekanismer, har det vist seg å være utfordrende å lage generaliserte dimensjoneringsregler for en Thomson spole aktuator.

Acknowledgements

I would like to express my gratitude to my supervisor Professor Kaveh Niayesh for giving me insight and sound guidelines on how to examine and handle the thesis. I also wish to thank Dr. Ivan Semenov for his insightful comments and help with the lab setup and testing. Also, a special thanks to Svein Erling Norum for being very helpful with the lab setup.

Table of contents

Figures

Tables

Chapter 1

Introduction

1.1 Relation to the Specialization Project

During the fall of 2021, I completed a specializations project with the title "Simulation and design of an electrodynamic Thomson coil actuator for fast mechanical switches", and a paper was written [1]. The specialization project gave me a solid understanding of the subject that was to be investigated further in the master's thesis, gaining insight into the application of the mechanism, the theoretical background and the method for modelling such a mechanism. The work from the specialization project is used in the master's thesis, further improving upon the model and making the model more realistic and robust.

The master's thesis contains material that is reused from the specialization project. Some of the material is modified but is based on the specialization project and will not be referenced further in the text. Instead, the original sources will be referenced. The sections that include reused material are listed below:

- Background and motivation in section 1.2
- Theoretical background 2.1-2.4
- Method 3.1 and 3.2

1.2 Background and motivation

In recent years there has been a political shift focusing on the contemporary climate change causing global warming. The leading cause of this rapid climate change is the emission of greenhouse gases. These greenhouse gasses are primarily carbon dioxide (CO2) and methane, and burning fossil fuels for energy is the main source of most emissions. Due to this, political agreements have been implemented to reduce the emission of greenhouse gasses and limit further global warming. In December 2015, The Paris Agreement, a legally binding international treaty on climate change, was adopted by 196 parties. The goal of the agreement is to limit global warming to below two degrees Celsius. To achieve this goal, the treaty states that the development of technology plays a big role, especially re-

garding energy production, as fossil fuels are the main cause of emissions [2]. Consequently, countries have promoted research by introducing incentives such as energy tariff guarantees to accelerate the research and development of green renewable energy technologies such as offshore wind farms and solar power, increasing the efficiency and making them viable alternatives to fossil fuel-based power plants for energy production. However, renewable power generation is often separated by large geographic distances from where the energy is consumed. This results in the challenge of transporting the renewable energy to the consumer with minimum transmission losses [3].

Historically the reasoning behind choosing to use an alternating current (AC) distribution system versus a direct current (DC) distribution system has been based on the cost of controlling and protecting these systems. As the technology for switching and protection of high voltage AC distribution systems is well established, AC systems have been dominating when it comes to multi-terminal systems. Apart from the challenges with controlling and protection in DC distribution systems, DC systems have significant advantages when compared with AC systems. Issues related to reactive power and harmonics play no role, and long transmission length does not cause large losses. As such point-to-point DC systems for transmission over long distances are already in use connecting grids together [4]. With the increase in the implementation of green renewable energy, the interest in high voltage direct current (HVDC) multi-terminal systems has increased significantly. Realizing a multi-terminal HVDC (MT-HVDC) system would enable easier integration of renewable energy sources (RES) and would have several advantages when compared to AC systems: reducing the number of terminals, stability (outage of one line does not interrupt the power flow), control (each terminal can operate at different power levels) and enabling asynchronous interconnections, making multi-terminal HVDC networks attractive. However, the realization of HVDC networks requires acceptable performance with respect to controllability, efficiency and reliability. This is strongly dependent on the availability of HVDC circuit breakers, making them a key technology for enabling such systems. In “HVDC Circuit Breakers: A Comprehensive Review”, a comprehensive review of the available technology of HVDC CBs has been completed. In the paper, the following types of HVDC CBs were investigated: passive, active, solid-state and hybrid DC circuit breakers. Of the different types, the hybrid DC CB shows the most promise, "combining mechanical and solid-state DC CBs, having the advantages, such as faster operation time, higher current breaking capability, and less power losses" [5]. Common for the hybrid DC CBs are the need for a fast mechanical disconnector. Both ABB and Alstom Grid have made working HVDC CBs using the current commutation scheme, making the opening speed of the mechanical disconnector the limiting factor when it comes to interruption time [5, 6]. Moreover, ABB has specifically used a Thomson drive to achieve fast opening times [7]. The technology of hybrid DC CBs are still in its infancy and are not commercially viable [5]. To reach the goal of making MT-HVDC a viable option, research towards design improvements of HVDC circuit breakers must be done to

further improve on current designs. Improving the Thomson drive by designing a high efficient electromagnetic drive with a faster opening time will improve the performance of hybrid HVDC CBs, reducing the need for current limiting inductors and further mitigating arcing, increasing lifetime and reliability [3]. The optimization and design of electromagnetic devices have traditionally been shown to be a complex and time-consuming process. But with the development of finite element method (FEM) based simulation software and the improvement of computation power, the design process cost and time have drastically been improved.

1.3 Scope

The purpose of the thesis is to investigate the Thomson coil drive as an ultra-fast disconnector for the use in HVDC CBs. A coupled multi-physics simulation model of the Thomson coil drive mechanism based on the FEM-software COMSOL Multiphysics shall be made. The model will be limited to the magnetic field force calculations, and the material will be assumed to be infinitely stiff. As such, solid mechanics will not be implemented, and masses will be modelled as lumped. To experimentally verify the general concepts of the simulation model, a prototype shall be made. From the verified simulation model, a parametric study of the Thomson coil shall be completed. To limit the simulation requirements, the parameters in the parametric study are limited to the capacitor's voltage and capacitance, the coil's number of turns and the armature width and thickness. Based on the parametric study and general understanding of the mechanism, a generalized iterative design process to size and optimize a Thomson coil drive shall be made.

Chapter 2

Theoretical background

2.1 Fundamentals on switching in DC systems

When comparing switching in HVAC systems with HVDC systems, there are several challenges in DC systems that in AC systems are less of an issue or completely avoided[5, 8]:

- Firstly, the lack of a naturally occurring current-zero crossing makes an otherwise manageable fault current very difficult to break. As such, the circuit breaker is required to generate its own current zero or turn off the current directly.
- Secondly, very large short circuit currents occur in HVDC systems during faults. This is due to the low line impedance of HVDC systems.
- Thirdly, the rate of rise (RoR) of the fault current in HVDC systems is very high compared to HVAC. Consequently, an HVDC breaker must interrupt the fault current typically within 5 ms.
- Fourthly, the magnetic energy in an HVDC grid is stored in the inductance of the system, and this energy must be dissipated through a mechanism in the HVDC breaker.
- Fifthly, the HVDC breaker must withstand residual overvoltages that occur after current interruption.

An equivalent circuit of a very simplified DC system is depicted in figure 2.1. The equivalent circuit contains an idealized DC source (V_n) and a line, represented as a resistor (R) and an inductance (L)–, a breaker, and a short circuit (V_{sc}).

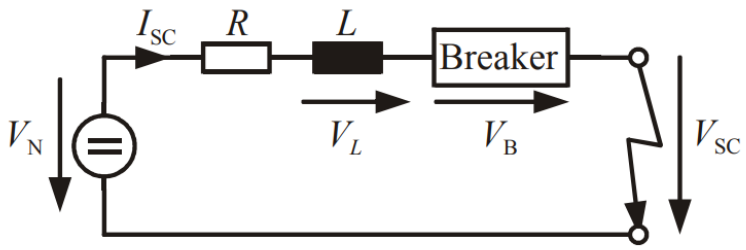

Figure 2.1: Equivalent circuit of DC system [4]

If the equivalent circuit is considered with an idealized short circuit and with the breaker closed, the following equation can be derived:

$$V_n = R \cdot I + L \cdot \frac{di_{sc}}{dt} \tag{2.1}$$

As an example, a system with a nominal voltage level set to 20 kV and the nominal current set to 2 kA can be considered when calculating the maximum short circuit current and the rise time of the current. HVDC grids fed by voltage source converters (VSC) do not have large inductive components like generators and transformers that are found in HVAC grids. These components limit the short circuit current in the HVAC system, but are lacking in the HVDC grid, making the short circuit current limited mainly by the resistance in the HVDC grid [4, 9]. For example, if an ohmic resistance of 10 $m\Omega$ is considered when calculating the maximum short circuit current, the resulting current will be 2000 kA. Furthermore, for the rate of rise of the current, if a cable length of 3 km with a total inductance of 1 mH is considered with a turn-off time of 20 ms, the maximum current will reach 400 kA. Naturally, this will not be reached due to the limitation of the short circuit power from the sources in the system. However, it demonstrates that fast switching actions for HVDC circuit breakers are essential to limit the fault currents in an HVDC system. As the suggested technology for HVDC grid application is VSC technology [8], one could argue that the VSC easily turn-off the load current within a few microseconds. However, this will lead to power loss in the entire grid for every single fault that occurs, making this an unacceptable strategy for a protection system in a DC grid [4].

2.2 State of the art - DC circuit breaker topology

Currently there are three main types of DC circuit breaker topologies [5]:

1. Resonance DC circuit breakers, these are mechanical and include active and passive resonance CBs
2. Solid-state DC circuit breakers, which only rely on power electronic switches
3. Hybrid DC circuit breakers, involving a combination of mechanical disconnectors and power electronics

2.2.1 Resonance DC circuit breakers

Figure 2.2 show the topology of a passive resonance CB. It consists of a mechanical switch in parallel with a resonance branch and an energy absorption/dissipation path. The mechanical switch interrupts the current when a current zero is generated by the capacitive-inductive resonance branch. The energy-absorbing branch consists of multiple metal oxide varistors (MOV) to absorb the energy stored in the system.

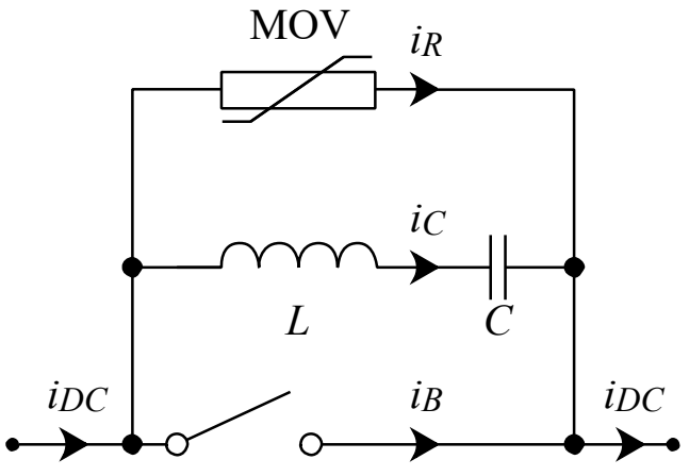

Figure 2.2: Typical topology of a passive resonance DC circuit breaker [5]

Under normal service, the mechanical switch is closed, and current passes through the current-carrying contacts. When an opening command is sent to the switch, the switch opens, and an arc is formed. Due to the commutation path, the voltage drop of the arc contributes to the current oscillations, causing the current to reach a current zero-crossing that eventually will extinguish the arc in the switch. After the arc is extinguished, the current will flow through the energy absorption path, dissipating residual magnetic energy in the system [8].

Resonance DC breakers have been proven to be too slow for use in MT-HVDC systems based on VSC technology due to the low action speed (in order of 30-50 ms) of the CBs when compared to the RoR of a typical HVDC system [5].

2.2.2 Solid-state DC circuit breakers

The topology of a solid-state DC CB typically consists of semiconductor components, either insulated bipolar transistors (IGBT) or gate turn-off thyristors (GTO) with a parallel MOV branch. Under normal service, the solid-state switch is turned on, and current flows through the semiconductor. When an interruption signal is sent to the breaker, the breaker switches off, forcing the current to flow into the

MOV branch. The MOVs limit the voltage over the breaker valves and then dissipate residual energy. Figure 2.3 shows an example of a typical solid-state breaker topology.

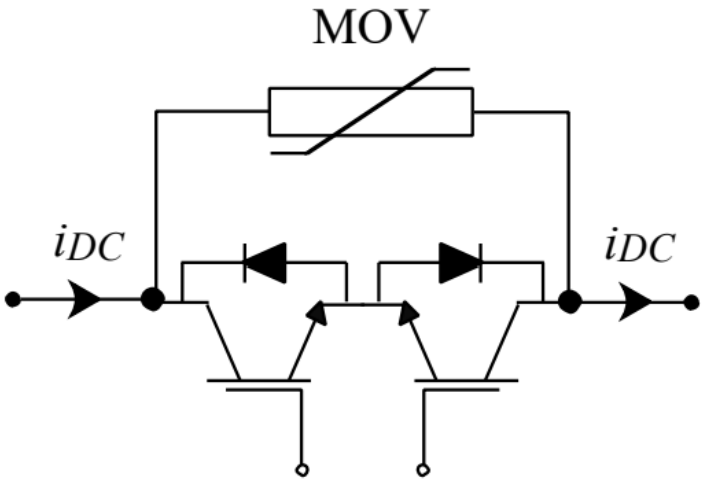

Figure 2.3: Typical topology of a solid-state DC circuit breaker [5]

More breaker valves can be placed in series to increase the voltage level of a solid-state CB. As solid-state CBs contain no moving parts opening speeds are extremely fast and have been proven to break currents in HVDC systems with the required speed. However, the high total cost and the high power losses due to the existence of permanent resistance makes them inconvenient for commercial use [5].

2.2.3 Hybrid DC circuit breaker

A typical topology of hybrid DC circuit break can be seen in figure 2.4 and consists of both semiconductor components and a mechanical switch. They combine the advantages of mechanical DC CBs and solid-state CBs, resulting in faster operation time (when compared to purely mechanical DC CBs), lower power losses and higher current breaking capabilities [10].

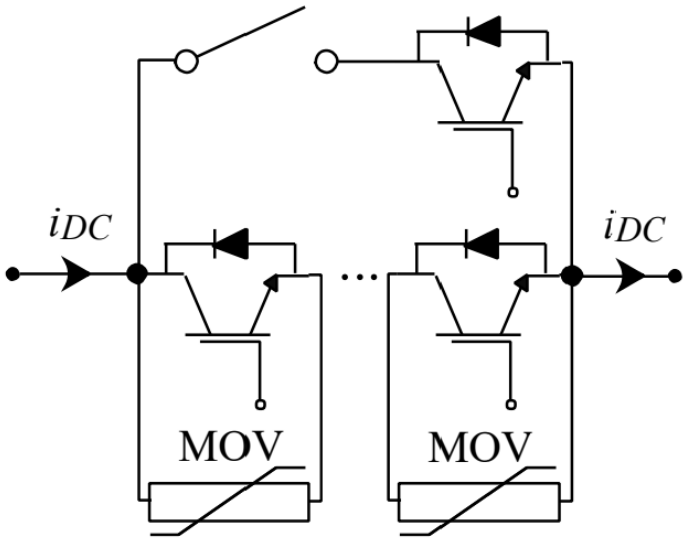

Figure 2.4: Typical topology of a hybrid DC circuit breaker [5]

Under normal operation of the hybrid DC CB, the current flows through a low impedance path. The low impedance path contains a low-ohmic ultra-fast disconnector (UFD) in series with a load commutation switch (LCS). The LCS is a solid-state DC breaker, and its purpose is to commutate the current into the main breaker branch. Consequently, it is only rated for this purpose giving much lower resistance losses. During a fault event, the current is redirected to a solid-state valve, the mechanical switch is opened, and the current is interrupted like in a solid-state CB [4]. As semiconductor switches have much faster interruption speeds without requiring a current zero-crossing, the opening time of the mechanical switch will be the limiting factor for hybrid DC CBs. Therefore, improving the speed of the opening mechanism of mechanical switches in hybrid CBs will be an important factor when designing future hybrid circuit breakers for MT-HVDC systems, thus making UFD a key component for the realization of this circuit breaker topology. The technology for HVDC CBs is still in its infancy, and the number of HVDC CBs in service is limited [5]. Nevertheless, some promising designs of hybrid HVDC CBs from ABB and Alstom Grid are developed and can be seen in figure 2.5 and 2.6, respectively.

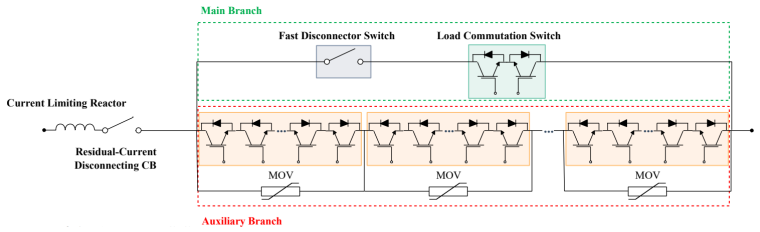

Figure 2.5: Hybrid HVDC circuit breaker topology from ABB [8]

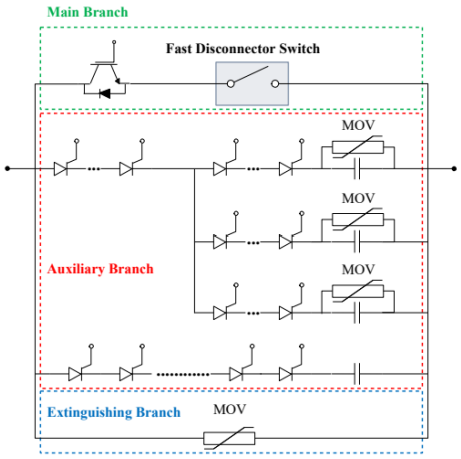

Figure 2.6: Hybrid HVDC circuit breaker topology from Alstom Grid [5]

The main difference between the two is that the ABB HVDC CB uses IGBT switches, giving it faster switching but less tolerance to high peak currents [11]. The Alstom Grid HVDC CB uses thyristors that tolerate higher fault currents when compared to IGBTs. However, they are harder to control, and in addition, they require a capacitor in series to help reduce the DC fault current to zero [12]. The ABB HVDC CB is suitable for systems that require fast current interruption capabilities, and Alstom Grid HVDC CB is useful in HVDC systems where longer time delays are required [5]. Common for both is that they require a fast disconnector switch in the main branch to function, and for this, UFD technology is required.

In HVAC CB technology, the driving mechanism alternatives have been hydraulic, pneumatic, or spring-operated systems. Spring-operated circuit breakers use one or several powerful springs as the driving mechanism. The springs are charged by an electric motor, and during operation, the springs are released, resulting in movement of the contacts. For the hydraulic and pneumatic systems, the energy is released by opening valves, releasing the energy stored in the system [13]. The opening speed of these driving mechanism has been sufficient for HVAC CBs, but are too slow for HVDC CBs. Therefore alternative driving mechanisms are needed in UFD that shall be used in HVDC CBs, such as the Thomson coil drive mechanism.

2.3 Electromagnetism

As the source of the force of the driving mechanism comes from electromagnetic phenomena, it is natural that some of the important concepts of the electromagnetic driving mechanism are mentioned. Generally, all electromagnetic devices can be described by Maxwell's equations. For magnetoquasistatic analysis, the change in electric flux density is assumed to be zero. A criterion for quasistatic analysis to be valid is that the currents and electromagnetic fields vary relatively slowly, meaning that the dimensions of the structure are small compared to the wavelength [14]. Lorentz force is classified under the subfield of magnetoquasistatic. As such, Maxwell's equation can be rewritten in the following manner:

$$\nabla \times \mathbf{H} = \mathbf{J} = \rho(\mathbf{E} + \mathbf{v} \times \mathbf{B}) + \mathbf{J_e} \tag{2.2}$$

$$\nabla \times \mathbf{E} = -\frac{\partial \mathbf{B}}{\partial t} \tag{2.3}$$

$$\nabla \cdot \mathbf{B} = 0 \tag{2.4}$$

$$\nabla \cdot \mathbf{D} = \rho \tag{2.5}$$

$$\nabla \cdot \mathbf{J} = 0 \tag{2.6}$$

For Maxwell-Ampère's law given in equation 2.2, J_e is an externally (e.g given from an electric circuit) generated current density, and $\mathbf{v}$ is the velocity of the conductor [14]. Equation 2.3 is Faraday's law, equation 2.4 and 2.5 is Gauss's law and Gauss's magnetic law respectively. These equations formulate the governing equations for the magnetic fields physics module used in COMSOL multiphysics.

2.3.1 Faraday's law

According to Faraday's law, electromotive force (emf) is given by the rate of change in the magnetic flux. Thus if a changing magnetic field passes through a loop of conductive wire, it will induce an emf, resulting in an electric current in the loop. Then naturally, the opposite will occur; if a time-varying electric current is sent through a loop of wire, a time-varying magnetic field will occur around the wire in the loop. This means that for generating large time-varying magnetic fields in coils, the $\frac{di}{dt}$ of the current is an important parameter [15].

2.3.2 Eddy currents

Electrically conductive materials that are in the proximity of a time-varying magnetic field will have loops of electrical currents induced within the conductive material called eddy currents. Due to Lenz's law, the eddy currents circulate such

that they create a magnetic field that opposes the change in the magnetic field of the source.

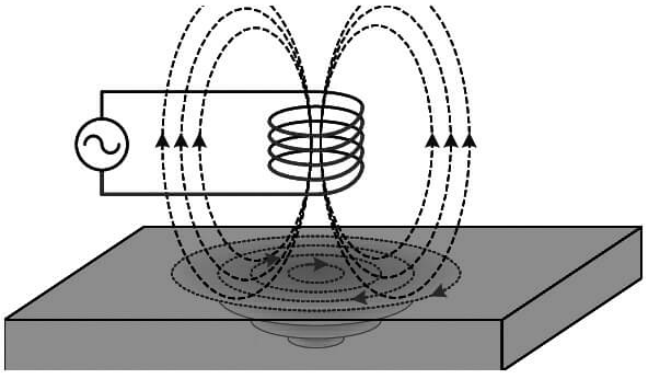

Figure 2.7: A solenoid inducing eddy currents in a conductive material [16]

As these currents flow in a direction opposite to the currents that induce them, the magnetic field generated by the eddy currents tends to cancel the penetrating magnetic field of the source, thereby reducing the inductance of the system [17]. The system can be modeled as an electrical circuit model with two inductors with mutual inductances, as seen in figure 2.8.

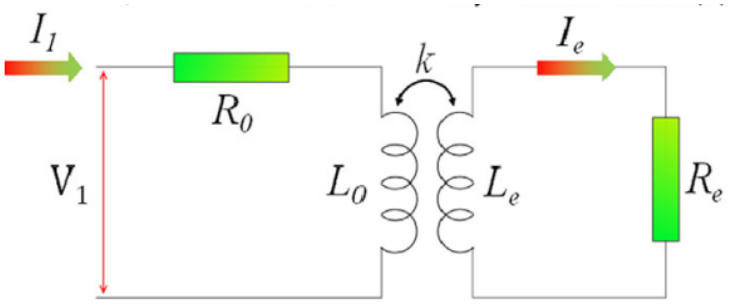

Figure 2.8: Simple electric circuit model of a coil magnetically coupled with the surface of a conducting material [16]

The total inductance of the system is dependent on the coil's parameters, the armature's conductivity, shape, and size, as well as its proximity to the coil. This means that as the air gap increases, the magnetic coupling between the armature and the coil decreases, resulting in an increase in the system inductance as the gap increases [3].

2.3.3 Skin effect

The skin effect is the tendency that high-frequent currents will flow in the outer layer of a conductor. The current density will be the largest near the surface of the conductive material and will decrease exponentially with the depths in the material. The skin effect is prevalent in eddy currents, and the eddy currents will concentrate at the surface of the material near the source of induction. The eddy currents flowing in the material generate a magnetic field that opposes the primary magnetic field, reducing the net magnetic flux, and decreasing the magnitude of the current as the depth increases. The standard depth of penetration can be calculated with the following equation and gives the depth at which the eddy current density has been decreased to $1/e$ or approximately 37 %,

$$\delta = \frac{1}{\sqrt{\pi f \mu \sigma}} \tag{2.7}$$

f represents the current frequency of the source of induction, μ and σ is the magnetic permeability and electrical conductivity of the material, respectively. [17, 18]

2.3.4 Lorentz force

The Lorentz force is the electromagnetic force that drives the TC actuator and can be defined by the following equation:

$$\mathbf{F} = q(\mathbf{E} + \mathbf{v} \times \mathbf{B}) \tag{2.8}$$

It is the force acting on an electric charge q of the subatomic particles that carry them, with a velocity of $\mathbf{v}$, due to an external electric field $\mathbf{E}$ and magnetic field $\mathbf{B}$. The term Lorentz force refers to both the electric force in the formula, $q\mathbf{E}$ and the magnetic force, $q(\mathbf{v} \times \mathbf{B})$ [19]. Often in the literature, the Lorentz force only refers to the formula for the magnetic force. Further, to make the equation applicable to a continuous charge distribution in motion, the equation becomes:

$$d\mathbf{F} = dq(\mathbf{E} + \mathbf{v} \times \mathbf{B}) \tag{2.9}$$

Resulting in the formula for force density:

$$\mathbf{f} = \rho(\mathbf{E} + \mathbf{v} \times \mathbf{B}) \tag{2.10}$$

Multiplying the charge density ρ with the velocity $\mathbf{v}$ results in current density J, giving the resulting equation for the force density from the Lorentz force:

$$\mathbf{f} = \rho\mathbf{E} + \mathbf{J} \times \mathbf{B} \tag{2.11}$$

To calculate the total force, the volume integral over the charge distribution must be calculated as such:

$$\mathbf{F} = \iiint (\rho\mathbf{E} + \mathbf{J} \times \mathbf{B}) d\mathbf{V} \tag{2.12}$$

In the Magnetic Fields interface in COMSOL, a predefined domain-level variable for calculating the Lorentz force exists. This is defined as:

$$\mathbf{F} = \mathbf{J} \times \mathbf{B} \tag{2.13}$$

Note that this is for force calculations in conducting domains. For force calculations in non-conducting domains, a more general method is used: integrating the Maxwell stress tensors. [14, 20].

2.4 The Thomson coil drive mechanism

A Thomson coil can be used as an electrodynamic drive mechanism for fast opening switches. A schematic outline of a Thomson coil arrangement can be seen in figure 2.9.

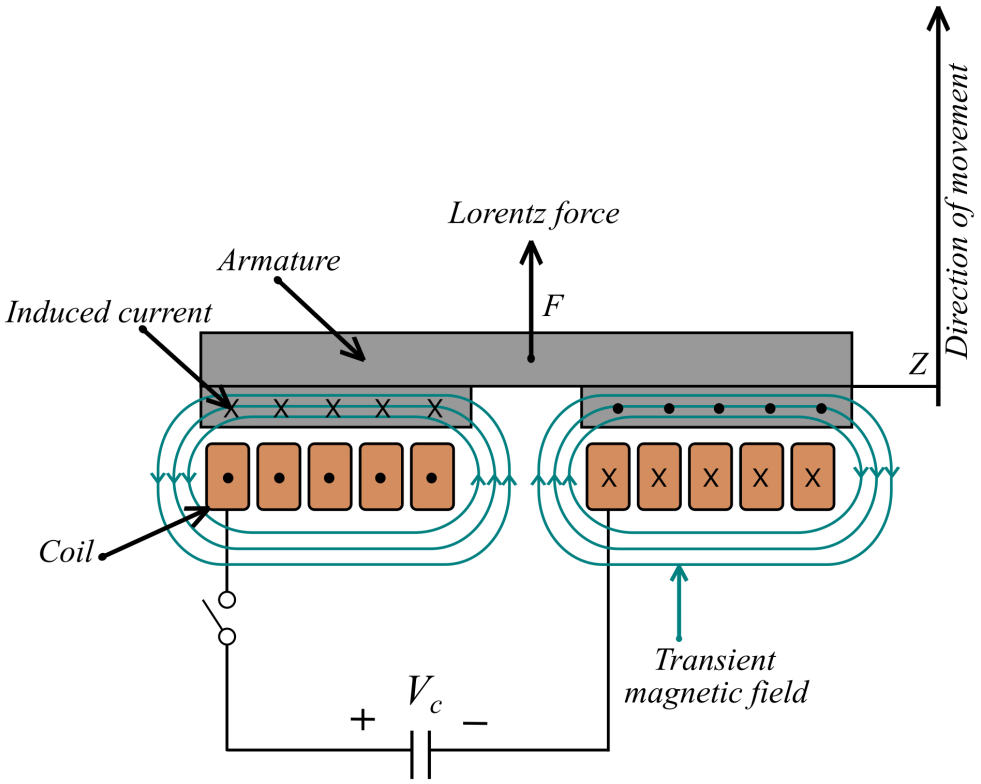

Figure 2.9: Schematic outline of a Thomson-coil arrangement

The Thomson coil consists of a flat multiturn spiral coil paired with an electrically conductive material placed above the coil, known as the armature. The armature can be attached to a push/pull rod which is used to actuate the electrical contacts in the switchgear, or the armature itself can act as the electrical contacts of the switchgear. A large current pulse is needed to achieve the fast

opening of the switchgear. This is achieved by having a large, charged capacitor bank that is discharged when the switchgear is triggered to open. This will, in turn, send a large current through the flat coil generating a rising magnetic field. This magnetic field will induce azimuthal rotating (rotating horizontally with reference to the flat coil) eddy currents of the opposite direction that opposes the increase of the time-varying magnetic field. The product of the induced currents, together with the radial component of the magnetic flux density in the armature, results in an axial repulsive force [3]. The coil is fixed in place, and the armature is free to move, resulting in movement of the armature and, in turn, the push/pull rod. From an electric circuit theory point of view the mechanism can be seen as an RLC circuit. The main factors that will affect the rise time of the coil current is the systems inductance and capacitance [3]. For RLC circuits the resonance frequecy is given by the following equation [21]:

$$f_{res} = \frac{1}{2\pi\sqrt{LC}} \tag{2.14}$$

The frequency of the coil current will be dependent on the capacitance of the energy source as well as the dynamically changing inductance of the system. When the air gap increases, the inductance increases resulting in a lowered current frequency. A low current frequency can cause the armature to move away prematurely from the coil before the coil current has reached its peak. As the armature moves away from the coil, the magnetic coupling between the armature and coil is lowered, reducing the eddy currents induced in the armature. The lowered magnetic coupling and induced eddy currents result in a significant loss in the forces between the coil and armature. Figure 2.10 shows a comparison of the force experienced by the armature when the armature is locked in place vs. when the armature is free to move. The area of the force curve represents the impulse that the armature experiences and shows the lost impulse force due to the increase in the air gap.

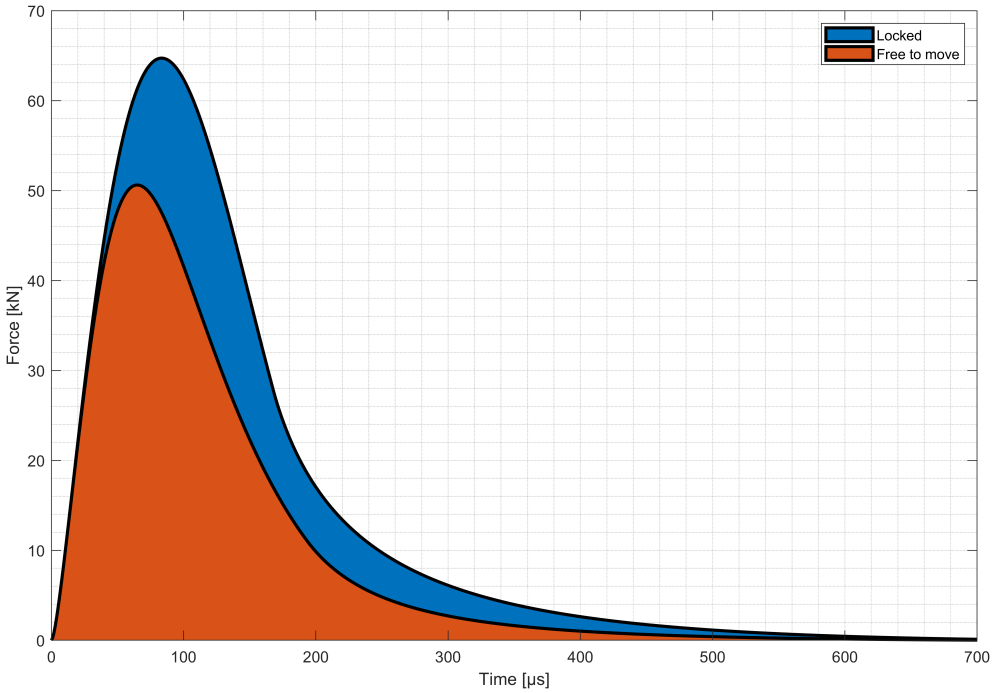

Figure 2.10: A comparison of the force experienced by the armature when locked and when allowed to move. The area of the force curve represents the impulse that the armature experiences and shows the lost impulse force due to the increase in the air gap.

Chapter 3

Method

3.1 The FEM models

Multiple simulation models have been made using COMSOL Multiphysics 5.6. A simulation model to represent the prototype was made to experimentally verify the principles behind the model. Further, several models for the parametric study were made with the parameters that are studied in mind. The models are based on the model built during the fall of 2021 for the specialization project. The models have been improved upon, including making a model where the coils are represented as a single conductor coil, improving the realism of the current density distribution in the coil. Generally, the models can be divided into two parts, the electric circuit model and the FEM model, which are then coupled together during simulations. The components modeled in the electric circuit are independent from the dynamically changing parts of the model and can be modeled as lumped elements. The components that are a part of the electric circuit model are the electrical source, in this case, a high-power capacitor, the free-wheeling diode, the measuring shunt, and the cable leads of the setup. As the resistance and inductance of the magnetically coupled coil and armature of the TC are nonlinear and will change dynamically, they will be modeled using a FEM model, simulating the inductance and resistance for each time step. A representation of how the electric circuit is coupled with the FEM model can be seen in figure 3.1.

The capacitor is modeled as a capacitance in series with its effective resistance. For the switch, leads, and the measuring-shunt, the impedance is lumped together, represented as $\mathbf{R_{Stray}}$ and $\mathbf{L_{Stray}}$, and the diode got model parameters implemented as well.

3.1.1 The electic circuit in COMSOL

The electric circuit in COMSOL uses Kirchhoff's conservation laws and solves for voltages, currents, and charges associated with the circuit elements [14]. The elements that are implemented in the COMSOL model are the elements from the circuit seen in figure 3.1. All the elements are implemented as basic circuit com-

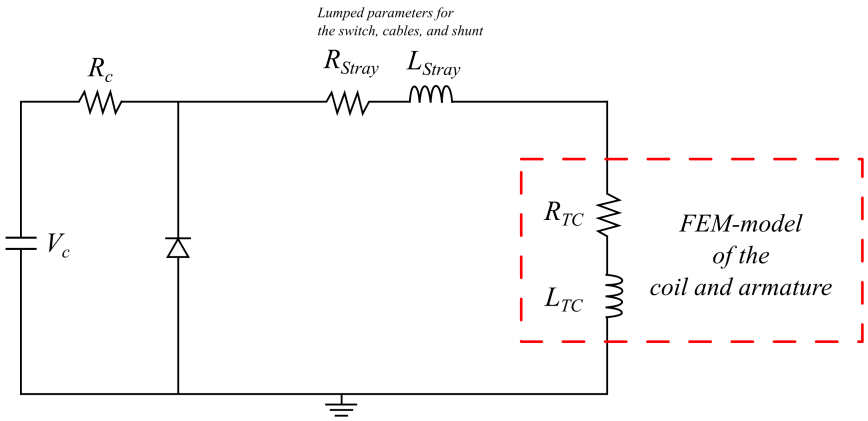

Figure 3.1: A representation of the electrical circuit coupled with the FEM model, $\mathbf{R_{TC}}$ and $\mathbf{L_{TC}}$ representing the dynamically changing resistance and inductance of the armature and coil

ponents that are connected to nodes. A switch is not added to the circuit. Instead, the capacitor is pre-charged and starts discharging instantaneously when the simulation is started. The connection between the electric circuit and the FEM model is achieved by an "External I vs. U" feature. This allows the external electric circuit to be the source for the coil excitation of the TC in the FEM model.

3.1.2 Geometry and material

A TC-actuator is an axially symmetric device allowing for the use of 2D-axisymmetric space dimension when simulating, avoiding the need for 3D-simulations, reducing the computation time of the simulation significantly. The geometry of the TC-actuator is defined as 2D-elements that are rotated around the axial line of symmetry. The coil, armature, and push/pull rod are defined with their respective materials, and an air domain is defined around the component. The material properties are taken from the COMSOL material library. The geometry will differ for each model depending on what they are representing and their usage. The main differences between the models would be if the coil is modeled as a homogenized multiturn coil or as several single conductors that are electrically coupled, representing a coil. The 2D geometry of a model with a homogenized multiturn coil can be seen in figure 3.2a, and the resulting 3D geometry can be seen in figure 3.2b. It is clear from the model that the coil is modeled as one homogeneous element.

The 2D geometry of the single conductor coil model can be seen in figure 3.3a, and the resulting 3D geometry can be seen in figure 3.3b.

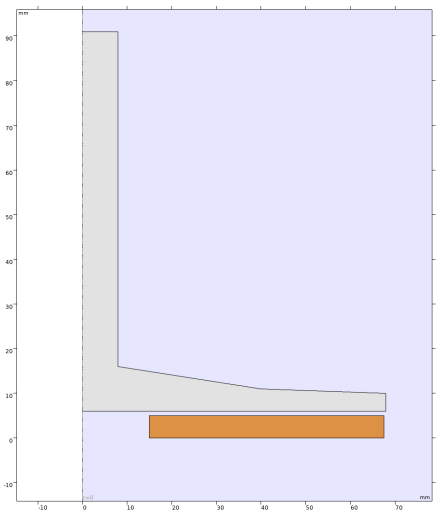

(a) 2D geometry of the homogenized multiturn coil model

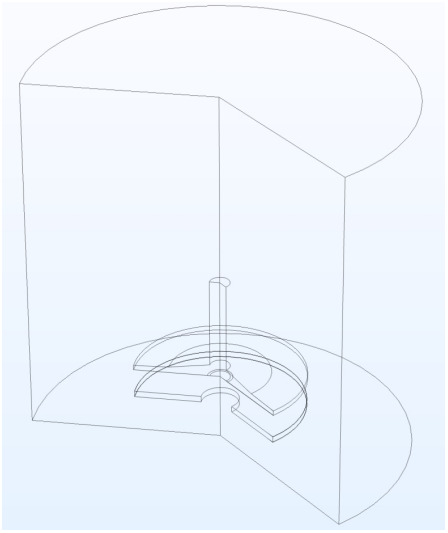

(b) The resulting 3D geometry of the homogenized multiturn coil model

Figure 3.2

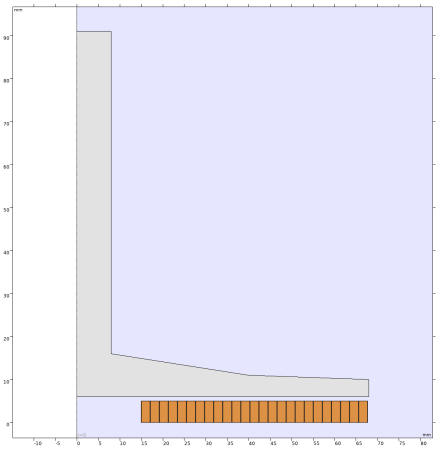

(a) 2D geometry of the single conductor coil model

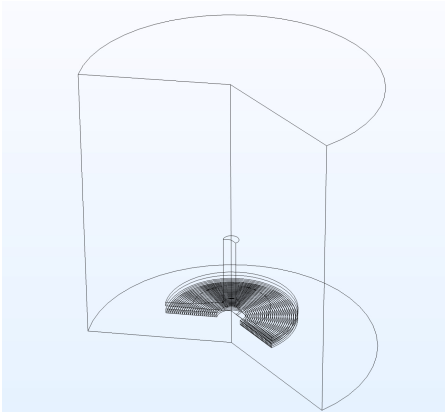

(b) The resulting 3D geometry of the single conductor coil models

Figure 3.3

3.1.3 Magnetic fields

The magnetic field interface is a major part of the physics in the model. The physics solves for Maxwell's equations formulated as magnetic vector potential as mentioned in the theory. How the coils are defined in the magnetic fields component is dependent on the model type, and is the main difference between the two types of models.

Homogenized multiturn coil model

The coil of the TC is defined as a homogenized multiturn coil representing the wires of the coil wound together but separated by an electric insulator, forcing the current only to flow in the direction of the wires. The number of turns is defined by the homogenized multiturn conductor, and the conductivity of the coil is given by the material. The coil wires cross-section area is calculated from the total area of the coil multiplied by a fill factor and divided by the number of turns:

$$a_{wire} = \frac{a_{coil} \cdot k_{fill}}{N} \tag{3.1}$$

The excitation of the coil is defined by the "External I vs. U" from the electric circuit, coupling the FEM model with the electric circuit model. The armature is defined as a single conductor coil letting the current flow freely in the material. The rest of the domain is defined by an Ampère's law node, either for a solid or non-solid domain separately. There is also a force calculation node available in the magnetic field interface, which is explained in the calculations section. The homogenized multiturn coil model makes it very easy to change the geometry and number of turns as long as the wire cross-section is defined such that it changes with respect to the coil area and the number of turns, as seen in equation 3.1. Making it a useful model for parametric studies where the coil parameters are rapidly changed. Due to the way the coil is defined, the accuracy of the model might not be as good as a single conductor model. This is due to the way the current density in a homogenized multiturn coil is defined. The current density will be completely homogeneously distributed, as seen in figure 3.5a. This is not the case for actual coils where the current will be affected by the skin effect, changing the high-frequency resistance of the conductor during the simulation [18].

Single conductor coil model

The way the single conductor coil model differs from the multiturn homogeneous coil model is the way the coil is defined. Each individual turn of the coil geometry is drawn in the model and defined as a single conductor coil letting the current flow freely in the material. Each coil is defined by an individual "External I vs. U" feature for each turn. Next, the circuit needs to be expanded to implement the coil into the electric circuit. The expanded electric circuit is shown in figure 3.1, where $\mathbf{R_{TC_N}}$ and $\mathbf{L_{TC_N}}$ represent the dynamically changing resistance and inductance of each individual turn in the coil with respect to the armature. The current can now flow freely in the material, and the resulting current density can be seen in figure 3.5b. The effects of the skin effect is apparent, the current density is larges near the surface of the conductors and close to zero in the center.

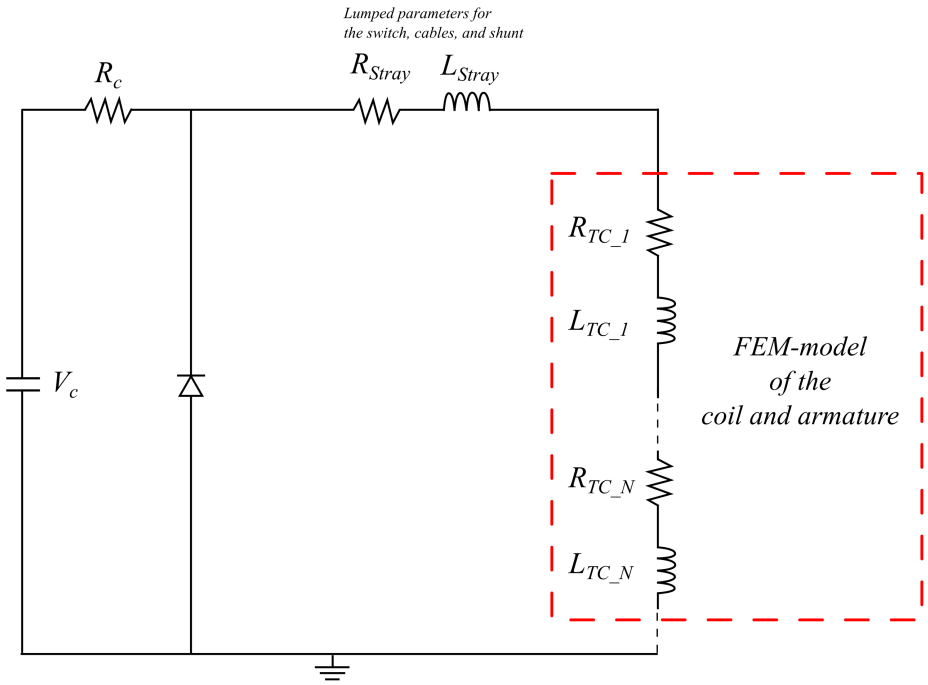

Figure 3.4: A representation of the electrical circuit for the single conductor coil model and how it is coupled with the FEM model. $\mathbf{R_{TC_N}}$ and $\mathbf{L_{TC_N}}$ represent the dynamically changing resistance and inductance of each individual turn with respect to the armature.

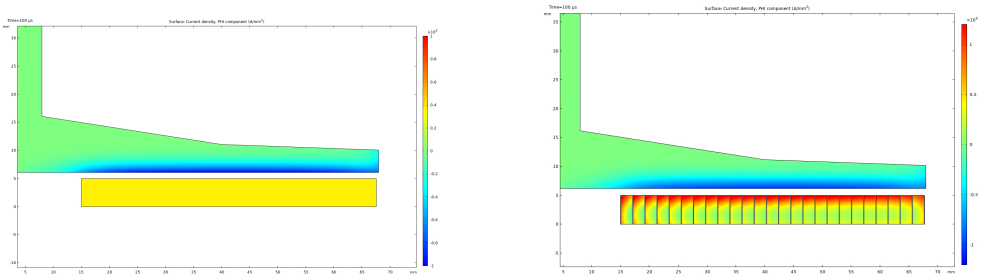

(a) Homogenized multiturn coil **(b)** Single conductor coil

Figure 3.5: The current density at 100 μs.

3.1.4 The mesh

The finite element method (FEM) divides the domains into a finite amount of elements of nodes that form elements that will be solved for. The nodes are solved and the areas between the nodes are interpolated [22]. Therefore, generating a good mesh is essential to get accurate results. The most critical part of the mesh

would be the air gap between the coil and the armature itself, as this is where the magnetic flux density is the largest. In addition, for the parts where a high current density is expected, a fine mesh with high quality is required to get an accurate current distribution. As such, the mesh size and distribution for the air gap, armature, and coils are specified, as seen in figure 3.6.

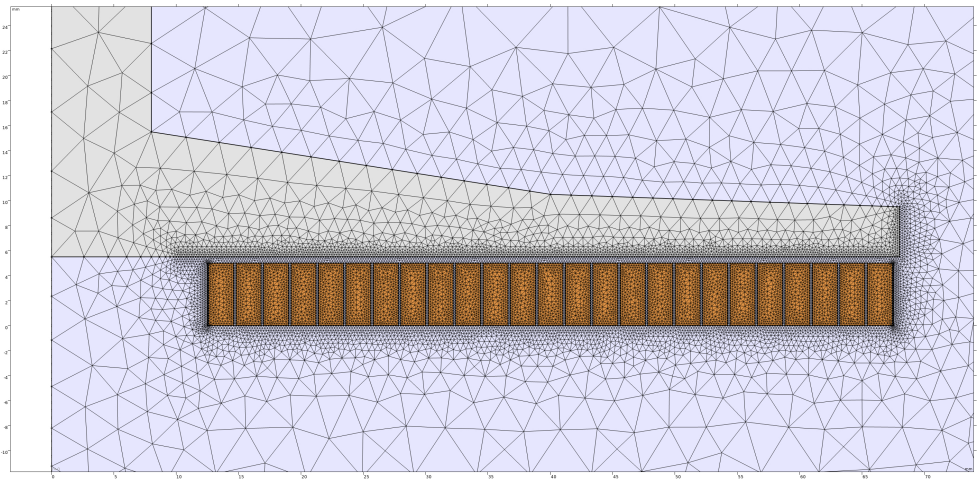

Figure 3.6: The figure shows the mesh of the single conductor coil model and the fine mesh of the air gap, armature and coil.

3.1.5 Moving mesh and automatic remeshing

The moving mesh is implemented by prescribing a deforming domain for everything that moves or is in any way deformed, in this case, the armature, rod, and air domain. The coil will be fixed in place with a fixed boundary. A prescribed mesh displacement on the boundaries of the rod and armature is implemented. This allows for the definition of the movement of the armature boundaries in the Z and R direction (in this case, only the Z direction is needed). Lastly, a normal mesh displacement is added to specify the displacement of the boundary in the reference normal direction where the boundary of the mesh at the symmetry line will be displaced. Now any function that defines the object's position can move the armature/rod in the mesh displacement boundary of the component.

A moving mesh causes stretching of the mesh, reducing the quality of the mesh elements. If the mesh is stretched too far, it will influence the simulation results to such an extent that they are unreliable. In the worst case, it will cause an inversion of elements resulting in an error, stopping the simulation. A way to avoid this is to implement an automatic remeshing feature that will remesh the model after a condition is met. The condition for remeshing could be specified by time steps, distortion, or mesh quality. As remeshing every timestep requires more computational power, the mesh quality is set as the condition for remeshing in these models. Figure 3.7a shows the time step right before a remesh is required. This is

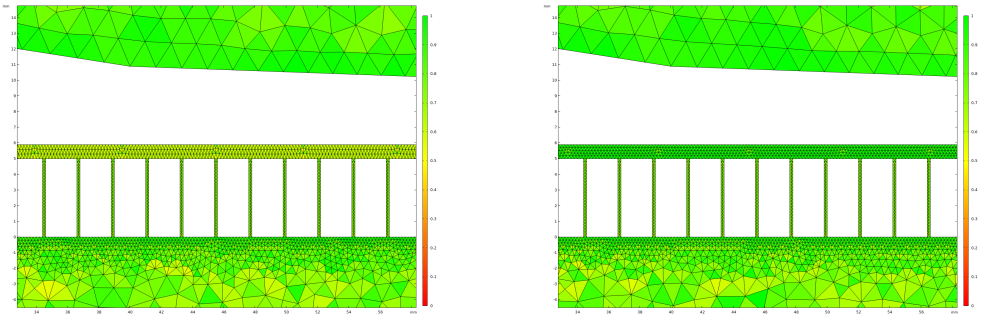

(a) Mesh of the air gap before the remesh.

(b) Mesh of the air gap after the remesh.

Figure 3.7: Mesh of the air gap at the timestep when a remesh is required with the minimum allowed skewness set to 0.4.

the maximum distortion of the mesh that is allowed before a remesh is required and is decided by the minimum skewness level set in the automatic remeshing feature. Figure 3.7b shows the remeshed model used in the next time step. Note that models with moving meshes might require more advanced solvers to get the model to converge.

3.2 Calculations in COMSOL

3.2.1 Current calculations

For every time step, the normal current density of the model is calculated from the Maxwell-Ampère's law stated in equation 2.2. To calculate the eddy currents that flow in the armature, a surface integral of the normal current density in the armature domain must be calculated. A surface integral for the required domains can be defined in the definition of the model. The current in the coil can also be calculated by the same method, but since it's connected to the electric circuit of the model, the coil current can simply be found from the circuit calculations.

3.2.2 Force calculations

There is a force calculation node in the magnetic fields interface that can be used to calculate the Lorentz force between the coil and the armature. The method uses the integration of the Maxwell's stress tensors over the exterior surface of the set domain [14]. The method gives access to the Z and R component of the electromagnetic force experienced by the domain. Due to the orientation and setup of the TC, the Z component is the only component needed, as the R component will be zero.

An alternative way to calculate the total force not using the force calculation node would be to take the volume integral of the force density of the instantaneous value of the Z component of the Lorentz force contribution as described in equation 2.12.

The inhomogeneous current density distribution in the armature and nature of the magnetic flux densities distribution from a flat coil will cause an inhomogeneous distribution of the force density as seen in figure 3.8.

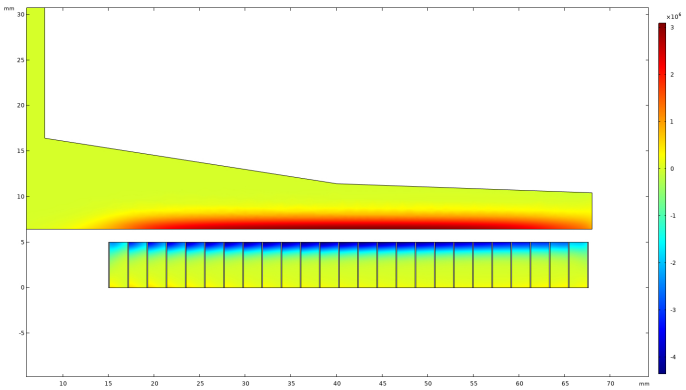

Figure 3.8: Inhomogeneous distribution of the force density in the coil and armature.

Since the magnetic field is unable to penetrate deep into the armature, most of the eddy currents are induced near the source of induction, resulting in high

force densities in the regions closest to the armature and coil.

3.2.3 Movement of the armature

To calculate the position of the armature at any time step in the simulation, the implementation of ordinary differential equations (ODEs) is required. This can be implemented from the global ODEs and DAEs interface. The armature's movement can be described by using Newton's second law of motion. Using acceleration as the source term for the equation and assuming that the armature is infinitely stiff, the ODE is derived by the following equations:

$$\sum F = m_{arm} \cdot a \tag{3.2}$$

$$\sum F - m_{arm} \cdot a = 0 \tag{3.3}$$

$$\frac{\sum F}{m_{arm}} - a = 0 \tag{3.4}$$

$$\frac{F_{lz} - m_{arm} \cdot g}{m_{arm}} - \ddot{x} = 0 \tag{3.5}$$

$$\frac{F_{lz}}{m_{arm}} - g - \ddot{x} = 0 \tag{3.6}$$

The calculated position of the armature is implemented in the moving mesh resulting in movement of the armature in the model. For each timestep, the force is recalculated with the new position of the armature, such that the force changes dynamically with respect to the new position. Most circuit breakers require some contact force to ensure satisfactory contact resistance [23]. This will cause a friction force during opening. Implementing this friction force in the simulation model can be advantageous. The friction force can be implemented with the same principles in the global ODEs and DAEs interface. For the case of the prototype, the armature was resting freely on the coil before opening. For the first few moments, the armature can move freely with no friction, and only at the end, when the end of the rod hits the stopper, the friction force is applied. As such, no friction term is needed for the simulation model in this case.

3.3 Parametric study

In the following section, some of the design parameters of a TC will be investigated. The study is divided into each component of the TC, and the specificed parameter for each component is investigated. The models used for the parametric study are adapted to each component or parameter, depending on how each parameter is changed. As such, the model might differ for each section depending on the parameter and component. How the model is changed will be explained in each section.

For a Thomson coil, the parameters that can be changed are limited to the energy source characteristics, the material, and the geometric shape of the TC. For the geometry of the armature and coil, the describing parametrization can be seen in figure 3.9, where A_w represents the armature width, A_t the armature thickness, C_w the coil conductors width, C_t the coil conductors thickness, C_{ir} the coils inner radius, and Tol represents the difference between the armature radius and the coil radius [24].

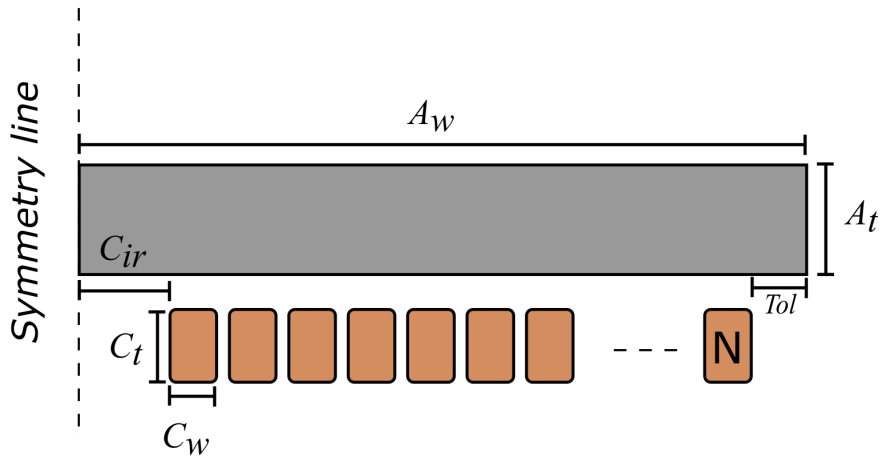

Figure 3.9: The parametric description of a generalized TC, where A_w represents the armature width, A_t the armature thickness, C_w the coil conductors width, C_t the coil conductors thickness, C_{ir} the coils inner radius, and Tol represents the difference between the armature radius and the coil radius.

The base geometry of the model for the parametric study can be seen in figure 3.10. The coil geometry is the same as the one used in the prototype, 25 turns, 5×2 mm rectangular conductors, and an enamel layer of 0.1 mm. This coil will be the base for all the parametric studies except when the coil itself got changing parameters. The armature geometry is changed to a more compact design to reduce the armature mass. The mass is based on its geometry and material and is, in this case, 0.251 kg and will be the base armature for the parametric studies where armature does not change.

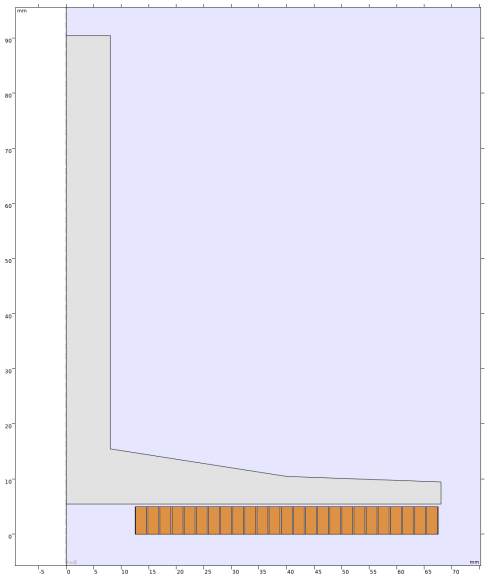

Figure 3.10: The base geometry for the simulation model used in the parametric study.

The efficiency of the energy transfer can be defined as how much of the electrical energy is transferred into mechanical energy. For a TC, the electrical energy input is the energy stored in the charged-up capacitor and can be defined as:

$$E = \frac{1}{2} C V_c^2 \tag{3.7}$$

The mechanical energy output of the TC would be the resulting kinetic energy of the armature and can be defined as:

$$E_k = \frac{1}{2} m v^2 \tag{3.8}$$

Then the efficiency would be:

$$\eta = \frac{m v^2}{C V_c^2} \tag{3.9}$$

Efficiency can be a good measure for optimizing a parameter of the TC. If the moving mass (the armature) is kept constant, then in most cases, the higher efficiency, the faster opening time of the armature. However, in some cases, the efficiency can be lower even though the opening time is faster within the limits set by the required opening distance. E.g., if the acceleration starts earlier and increases faster but lasts for a lower duration, it may result in a faster opening time but a lower end speed.

Opening time is a criterion that must be defined based on a desired opening distance. The distance may vary depending on the requirements of systems CBs. As an example, the speed requirements of an actuator for a UFD in a 320kV HVDC

grid is to separate the contacts by 50 mm in 2 ms [3]. For this parametric study, the opening distance is set to 50 mm.

Current characteristics of both the coil current and armature current will, in some cases, be interesting as the coil and resulting armature current are the source of the magnetic fields and Lorentz force for each case. In addition, the frequency and magnitude of the current can often give much information about the resulting opening time and efficiency and will therefore be discussed when relevant.

3.3.1 The energy source

The energy source for larger TCs would be high-power capacitors. The two variables that can be varied for capacitors are the charging voltage, V_c, and the capacitance of the capacitor, C. For any given TC, there would be an optimal energy source with regard to opening time and energy input. This means that if the energy input is limited to a maximum constant energy and the voltage and capacitance are varied with respect to each other, for that given energy and TC, an optimal voltage to capacitance ratio can be found.

To investigate how the voltage and capacitance of a capacitor affect a certain TC, the energy input is set to a constant of 500 Joules, and the voltage is varied from 300 V to 1200 V with increments of 100 volts. Table 3.1 shows the capacitance with respect to the voltage level for each simulation.

Table 3.1: The capacitance and voltage for the parametric study for a constant energy input of 500 Joules.

Voltage [V]	Capacitance [mF]
1200	0.694
1100	0.826
1000	1.00
900	1.23
800	1.56
700	2.04
600	2.78
500	4.00
400	6.25
300	11.1

3.3.2 The coil

The most important parameter for the parametric study of the coil is the number of turns. The inductance of a flat spiral coil is approximately proportional to the square of the number of turns: $L \propto N^2$ [25]. The inductance of the TCs system is mainly dominated by the coil. As such, when changing the number of turns, the current characteristics will change greatly. The coil size is based on the same one

used in the other parametric studies. The general geometric shape will stay as is (inner and outer radius and the thickness of the coil), but the number of turns and width of the conductors will change. The parametric study of the coil will use a model with a homogenized multiturn coil that can easily change the number of turns without changing the geometry of the coil. This is much more practical as the model geometry must be rebuilt and redefined for each change in the number of turns if a single conductor coil model was to be used. The number of turns will span from 5 to 50 with increments of 5, totaling in ten simulations with different turn values. The efficiency, opening time, and frequency will be plotted, as well as the total coil current for each simulation.

3.3.3 The armature

For the armature, the geometry of the armature itself is the parameter that can be varied, as well as the material. Generally, the goal of the armature is to induce as large eddy currents in the armature as possible with the smallest mass possible. For the armature material, the two contenders are copper and aluminum because of the electrical properties of the materials. It has been shown that even though copper can achieve higher current densities, the extra mass due to its greater density does not compensate for the extra force generated [3]. As such, only aluminum is considered in the parametric study. When considering the geometry of the armature, it can primarily be varied in two ways. Either the width or the thickness of the armature can be changed. The width should be at least as wide as the coil plus a small tolerance to maximize the induced current in the armature [24]. To see how the change tolerance affects the opening time and efficiency, the tolerance must be varied with the mass changing depending on the change in tolerance. For the simulations, the armature width is set equal to the coil width, and the tolerance is varied from -10 mm, up to 10 mm with 2 mm increments, giving a total of 11 simulations. The armature thickness was varied from 4 mm up to 22 mm, with 2 mm increments, giving a total of 10 simulations. The capacitor's capacitance is set to 1.00 mF, and the charge voltage is set to 1000 V, giving an energy input of 500 J.

Due to the high-frequent nature of the coil current and the eddy currents in the armature, the currents will be affected by the skin effect, and the depth of penetration decreases as the frequency increases [18]. Further, the relative magnetic permeability (μ_r) of aluminium is very close to air. As such, the magnitude of the eddy currents decreases exponentially with the dept of the material [17]. This reduces the current density drastically the further away the material is from the source of induction. This means that increasing the armature thickness does not necessarily increase the area with high current density efficiently.

For the parametric study of the armature, a simplified model of the armature is used. The rod is removed and modeled as a lumped mass and does not change with the change in parameters. The armature is cylindrical with a filleted edge, and the mass of the armature disc will change with the change in width or height.

The simplified model can be seen in figure 3.11. The simplified geometry is implemented to reduce computation time and to simplify the geometry to emphasize the change in the parameter.

To emphasize how the current density in the armature is affected by the change in its geometry, the simulations are divided into two cases. One case with the armature is locked in place, where the force, impulse, and armature current are investigated. And a case where the armature is free to move to investigate the change in opening time and efficiency due to the change in the armature geometry.

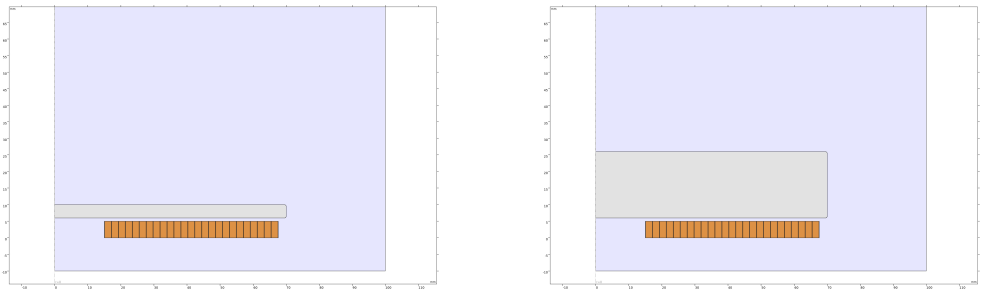

(a) Armature thickness set to 4 mm **(b)** Armature thickness set to 20 mm

Figure 3.11: The simplified armature model

It is important to note that an armature can not be indefinitely thin as it has to withstand the large Lorentz forces generated between the armature and coil. Especially if the armature is designed to carry an extra mass as load during opening. The thickness and shape of the armature must be considered when designing the geometry of the armature. The armature can not be permanently deformed during opening and elastic deformation will affect opening times. This has not been considered in this parametric study as the simulation models is to be considered infinitely stiff.

3.4 The prototype

The following chapter will describe how the complete prototype was realized and each part of the prototype in detail. During the spring of 2022, the planning and making of a prototype began. The prototype is to be used for experimental verification of the simulation model. It is not designed with optimization of the mechanism as the primary goal but instead with robustness and repeatability of measurements in mind. Several geometric options were considered, but only the final design will be presented here.

A picture of the armature and coil can be seen in figure 3.12, an electrical schematic of the setup can be seen in figure 3.13 and a picture of the wiring closet with the contactors, diode, bleeder-resistor and wires can be seen in figure 3.14. A schematic drawing of the different parts that were produced in the workshop can be found in appendix A.

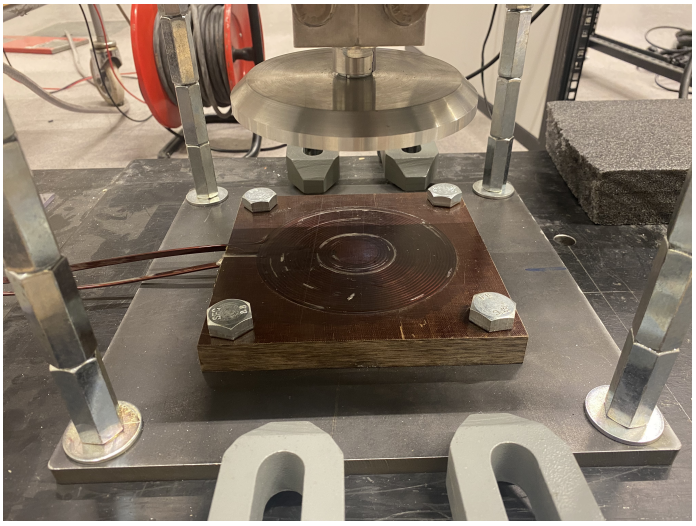

Figure 3.12: Picture of the coil installed in the rack

3.4.1 Energy source

The energy source for the prototype is a metallized polypropylene film capacitor with a capacitance of 2.38 mF with a maximum charging voltage of 800V from the supplier WIMA. The capacitor should have a large enough I_{max} to ensure that it can deliver the expected current for a capacitor with the stated characteristics. This capacitor has an I_{max} of 26 kA, which should be more than enough for this prototype. In addition, a metallized polypropylene film capacitor can withstand reverse polarities which can occur in the test setup, making it a relatively safe capacitor-type for the prototype test. The only available power supply at the time was a 600 V DC power supply from Delta Elektronika, giving the maximum test voltage for the prototype to be 600 V.

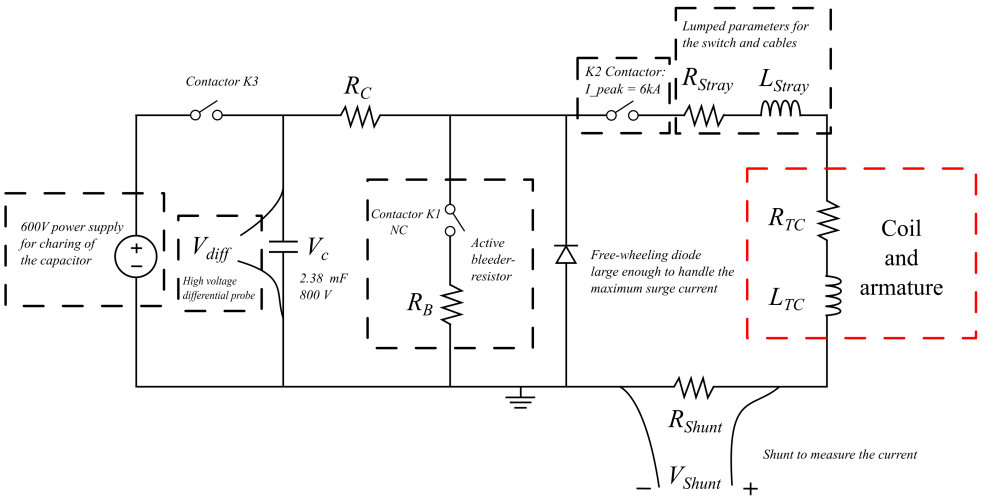

Figure 3.13: Electric schematic of the prototype setup

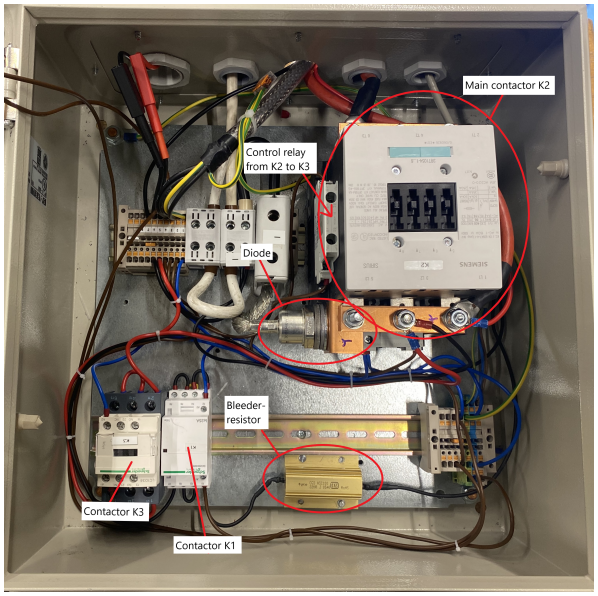

Figure 3.14: The picture shows the wiring closet with the different components marked. K3 is the contactor that connects the power supply, and K1 connects the bleeder-resistor if the capacitor fails to discharge. K2 is the contactor that acts as the main switch. The control relay from K2 will trigger K3 if K3 is still closed when K2 is triggered to be closed. This ensures that the power supply is disconnected after the capacitor is fully charged and K2 is triggered for testing.

3.4.2 Coil

The coil was designed to be a multiturn flat spiral coil with a rectangular copper conductor. The workshop had different-sized rectangular copper conductors available that are pre-coated with an enamel. A 5x2 mm conductor was chosen as the conductor size, with an 0.1 mm enamel layer on the copper conductor. The coil will undergo relatively high impulse forces during testing due to the Lorentz forces generated between the armature and the flat coil. Because of this, the coil needs a tightly fitted coil housing such that the conductors are not allowed to move. The material used for the coil housing was hard paper Pertinax. To estimate the coil radius, the following equation can be used:

$$C_r = C_{ir} + N \cdot C_w + 2 \cdot (N-1) \cdot e_w \tag{3.10}$$

Where C_{ir} is the inner radius, C_w is the conductor width, N is the number of turns and e_w is the enamel width [24]. For the prototype, an inner radius of 15 mm was chosen, and the number of turns was 24, giving an estimated coil radius of 67.6 mm rounded up to 68 mm. The coil was wounded on a lathe machine and then pressed into the housing. Due to a little extra space from the rounding up and a fairly tight fit, the number of turns ended up at 25 turns. A picture of the installed coil can be seen in figure 3.12. The dept of the housing was set to 5.3 mm, giving an extra 0.1 mm for the coil when pressed into the housing frame; this was to ensure that the coil is completely encased in the housing, giving a flush edge when filled up with protective glue.

3.4.3 Armature

The armature width should be equal to the coil width plus an extra tolerance. The tolerance is required to increase the induced currents in the armature, ensuring that the armature engulfs most of the magnetic field generated by the coil. However, increasing the width of the armature will increase the mass of the armature; hence there is an optimal tolerance for every case [24]. In this case, the tolerance was set to 2 mm, making the armature radius 70 mm. A bevel was made on the edge of the armature to give a sharp edge for measuring when using the high-speed camera. The armature material was aluminum. Aluminum has good current carrying capabilities as well as being relativity light. Alternatively, copper could be used since it has higher electrical conductivity. However, the increased mass of copper outweighs the force gained from the increased current in the material [3]. The total mass of the armature, including the rod, was 0.864 kg. A picture of the armature can be seen in figure 3.12, and the schematics can be seen in the appendix: A.

3.4.4 Rack and stopper

Very large peak forces (in the ranges of 20-30 kN) are estimated to take place during the testing of the prototype. As such, a robust rack is needed for the coil

and armature to be installed inn. In addition to this, a stopping mechanism to stop the armature from moving after testing is required. The stopping mechanism should not affect the armature before it has traveled the required closing distance. For this, a relatively primitive stopper block was made. The block is placed in the roof of the rack, and the rod has a conic shape at the end of the rod. When the mechanism is triggered to open, the armature flies vertically, wedging the rod into the stopper due to the elasticity of the aluminum. The stopper block is divided into two symmetric parts with bolts going horizontally through the block, locking them together when tightened. If the rod gets stuck, the bolts can be loosened to release the rod from the stopper. A picture of the rack with the armature stuck in the stopper can be seen in figure 3.15. The rack was mounted onto a large and massive metal frame that was leveled. This is to ensure minimal movement of the holding surface during testing, as the coil will undergo equal amounts of force as the armature during testing, pressing the coil against the floor of the rack. If the mounting surface flexes too much, the movement can affect the results of the measurements, making them inconsistent or invalid.

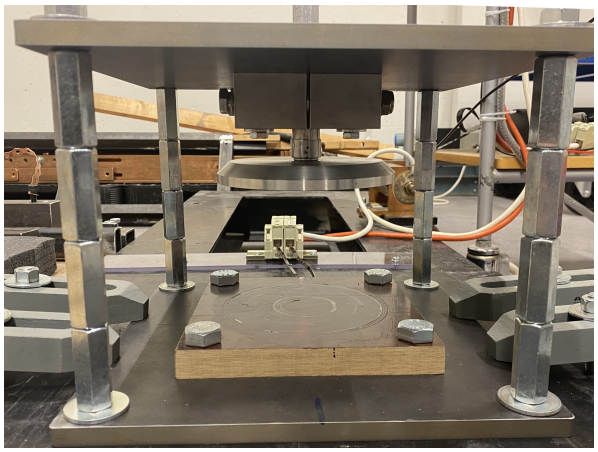

Figure 3.15: Picture of the rack and stopper with the armature stuck in the stopper

3.4.5 Main switch

For the main switch, the most important characteristics was that it was able to carry the large transient current and, at the same time, close fast enough such that it does not affect the transient current that it will carry. Naturally, solid-state semiconductor switches were considered as the closing time of such devices are virtually instantaneous. Both IGBTs and thyristors were investigated as potential switches, as well as using a large mechanical contactor switch as the main switch. It was hard to find IGBTs with large enough current carrying capabilities without becoming too expensive or impractical. As such, this option was scrapped. However, thyristors can carry much larger transient overcurrents making this a suitable option for the main switch. Two hockey-puck thyristors were ordered, and a trigger circuit for the thyristor was made. The plan was to first test the setup with the large contactor and then change it with the thyristor. One concern with using a contactor as the main switch was that it would vibrate too much when closing, causing poor contact during the initial closing of the contactor and giving high contact resistance. After a few tests, it became clear that the closing vibrations were minimal, and the contact resistance was satisfactory. Figure 3.16 shows the voltage over the capacitor in one of the tests and shows an expected voltage curve when compared to the simulations. Because of this, it was decided that there was no need to use the thyristor as the main switch because the contactor was working fine for its purpose in the testing of the prototype. All the later experiments were done with the contactor functioning as the main switch.

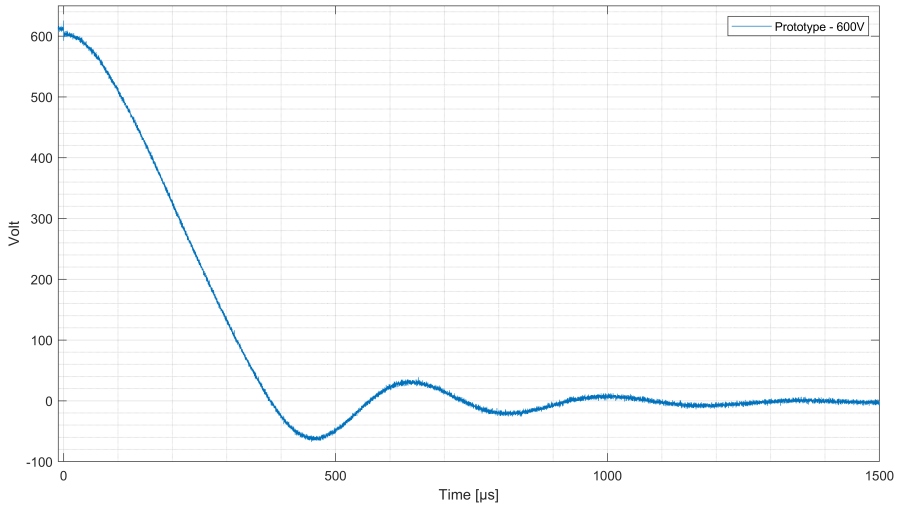

Figure 3.16: The figure shows the capacitor voltage from one of the tests with the mechanical contactor as the main switch.

It is important to note that for an actual implementation of the TC as an opening mechanism in fast mechanical switches, a contactor can not be used as the main switch for the coil current. This is because the contactor itself has a significant trigger delay from the fault opening signal to the actual closing of the contacts.

For an actual implementation, a solid-state semiconductor switch must be used to minimize this delay [8]. For the prototype, the delay in the measurements was avoided by triggering of the rising edge of the current, giving a negligible delay in the other direction.

3.4.6 Measuring methods

For measuring the different characteristics of the setup, some measuring equipment was needed. A diagram of the measuring setup can be seen in figure 3.17. An oscilloscope from Rohde & Schwarz was used to measure the electrical components and to trigger the high-speed camera. A high-voltage differential probe with a 500:1 ratio was used to measure the capacitor voltage during testing. To measure the coil current a 0.545 $m\Omega$ shunt resistor was used. The trigger time of the experiment was set to trigger from the rising edge of the current, and was set to trigger at 200 mV. This is equal to approximately 367 A. The trigger delay is minimal due to the nature of the fast rise time of the current. The most significant delay was at 300 V and was approximately 1.5 μs, which is so small that it can be counted as negligible.

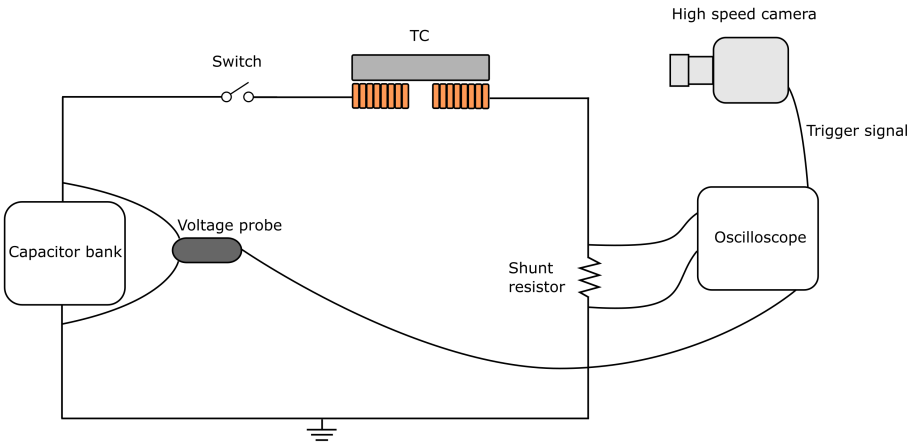

Figure 3.17: The diagram shows how the scope and high-speed camera are set up for measuring the prototype test setup. The oscilloscope is triggered of the rising edge of the shunt current, and the oscilloscope triggers the high-speed camera.

A high-speed camera from Photron was used to capture the movement of the armature. The camera's frame rate was set to 20000 FPS for most of the tests that were completed in the lab. The video resolution gets very low at very high frame rates and requires more lighting to capture a good picture. 20000 FPS is fast enough to capture the movement without losing too much resolution and keeping the picture from becoming too dark. Since the acceleration phase of the armature

is so short compared to the travel time (most of the acceleration is done in the first 400 μs), it was hard to capture enough frames to get a good measurement of the acceleration of the armature. To try and get a better measurement of only the acceleration phase, the camera was set to 64000 FPS, and the lens was moved and zoomed as close as possible to the armature such that only a small part of the movement was captured, giving a more accurate measurement of the acceleration.

Analyzing the footage

To generate usable data from the high-speed camera recordings, a Matlab script was implemented. The script uses a minimum eigenvalue algorithm to detect corner points of the grayscale input image, in this case, the high-speed camera footage, such that it can follow the detected feature points [26]. Figure 3.18 shows the feature points detected by the minimum eigenvalue algorithm in the chosen area at the base of the rod. A reference point of a known distance in the image is

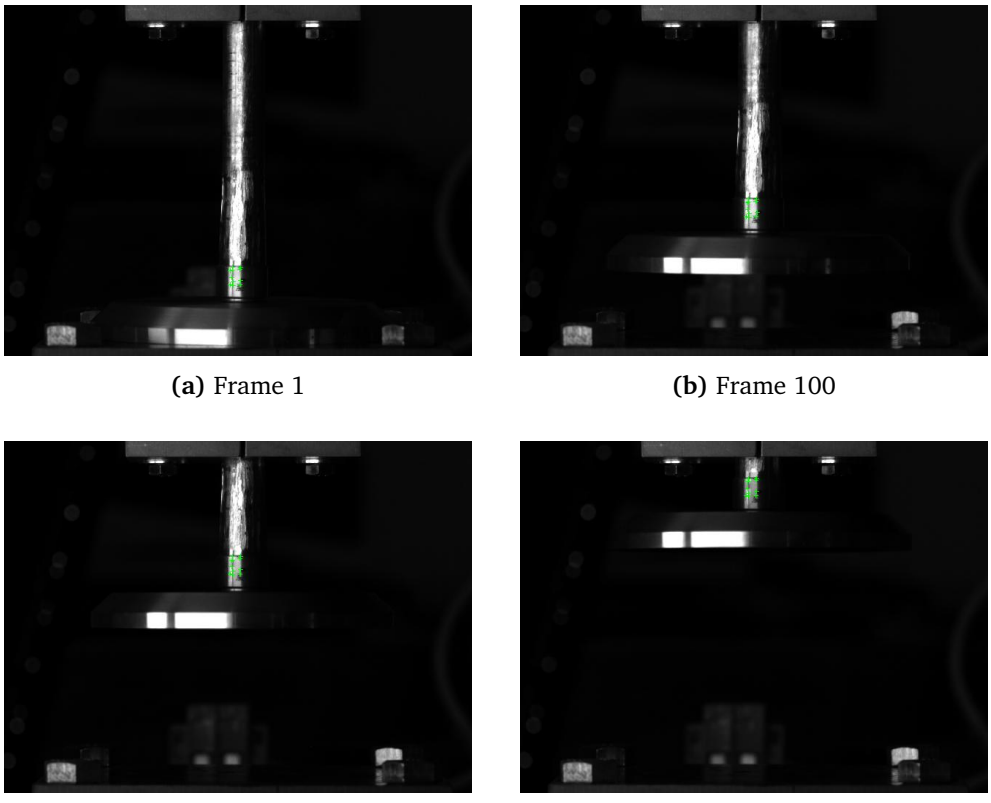

(a) Frame 1 **(b)** Frame 100

(c) Frame 200 **(d)** Frame 300

Figure 3.18: The four images shows the feature points detected by the minimum eigenvalue algorithm in each frame.

used to convert a pixel into a representative distance for one pixel, and the frame rate gives the change in time between each step. The movement of the feature

points can then be converted into distance moved per frame, giving the meters per second of the armature. The acceleration can then be calculated from the movement curve.

Some vibrations occur during testing causing the data to become slightly noisy. A smoothing filter is applied to the data to reduce the noise, and a plot of the raw data vs. the filtered data can be seen in figure 3.19.

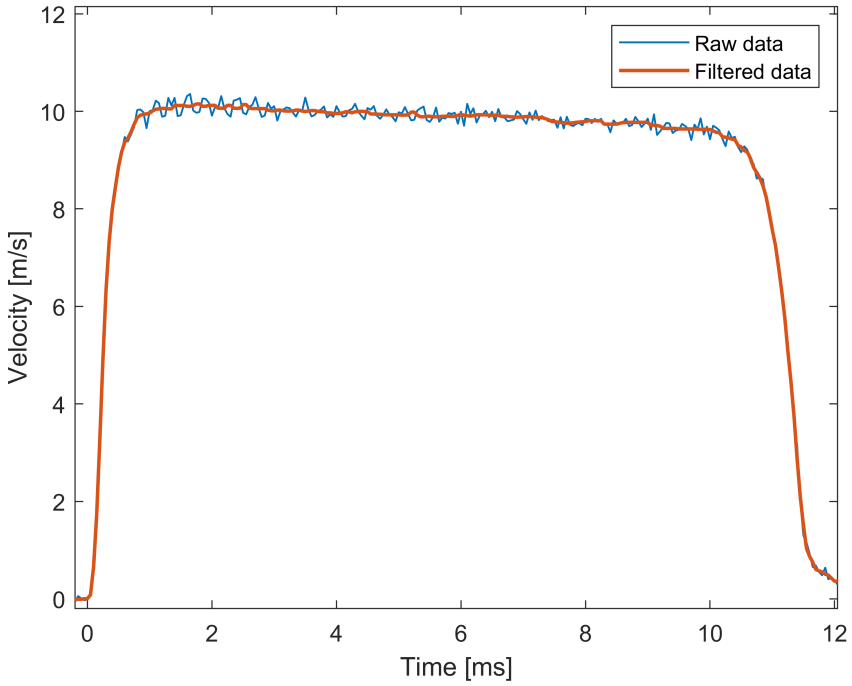

Figure 3.19: The figure shows the raw data vs. the filtered data of the armature speed.

Chapter 4

Results and discussion

4.1 Experimental verification of the simulation model

To verify the concepts of the simulation model, an experimental verification of the model was completed. The simulation model was modified to represent the prototype; the geometric shape and parameters were set to match the experimental setup, and the geometry of the simulation model can be seen in figure 4.1. A com-

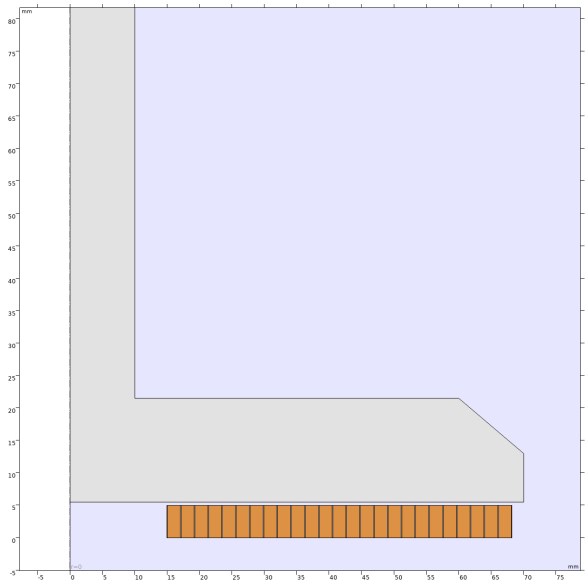

Figure 4.1: The geometry of prototype model in COMSOL.

parison of the simulation results vs. the experimental results was completed to look at potential discrepancies. The charging voltage of the capacitor was varied in increments of 100 V, from 300 V up to 600 V. Five experiments at each voltage level were conducted, and the capacitor voltage, coil current and movement of the armature were measured. The results from the different voltage levels of the five experiments were compared to check for repeatability and variations in the

measurements. In the 400 V data set, one small outlier was found to be large enough to be counted as an anomaly. Because of this, it was decided to remove this data set from the measurements, as the other four measurements had a much higher correlation, making it likely that the measurement was not correct. A plot of the movement of the armature from the five experiments can be seen in figure 4.2. The data set of all other measurements was kept as no other anomalies were found.

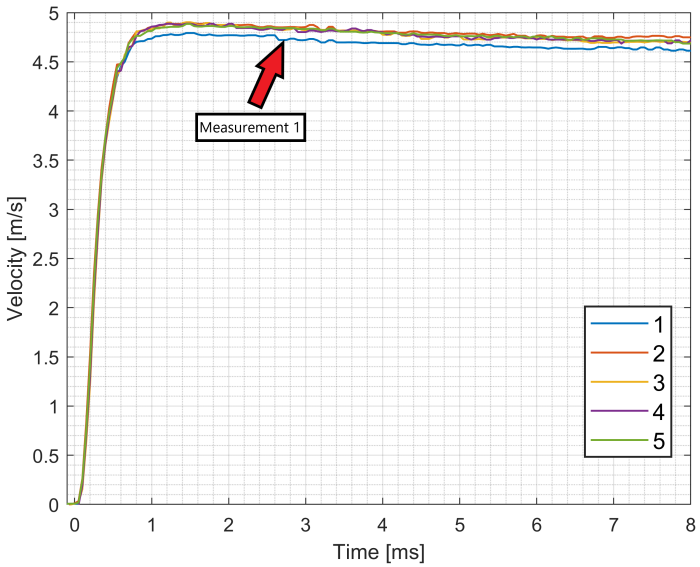

Figure 4.2: The measured armature velocity of the five experiments at 400 V, showing the outlier in measurement 1.

In the following subsections, a comparison of the experiment's measurement results and the simulation results are presented. The average value of each data point is calculated from the five data sets from each experiment, and the curves used in the comparison are the average values from the experiment.

4.1.1 Velocity

In figure 4.3, a comparison of the armature velocity obtained from the experimental measurements and the simulated armature velocity for the different voltage levels is presented. The dashed lines represent the experimental measurements, and the solid lines represent the simulations. The measured velocities coincide well with the simulated velocities. The velocity curves align at the initial acceleration phase, as well as after the initial acceleration has passed and constant speed is obtained. Indicating that the force that the armature experiences is similar to the simulated force, resulting in the similar velocity curves observed in the figure.

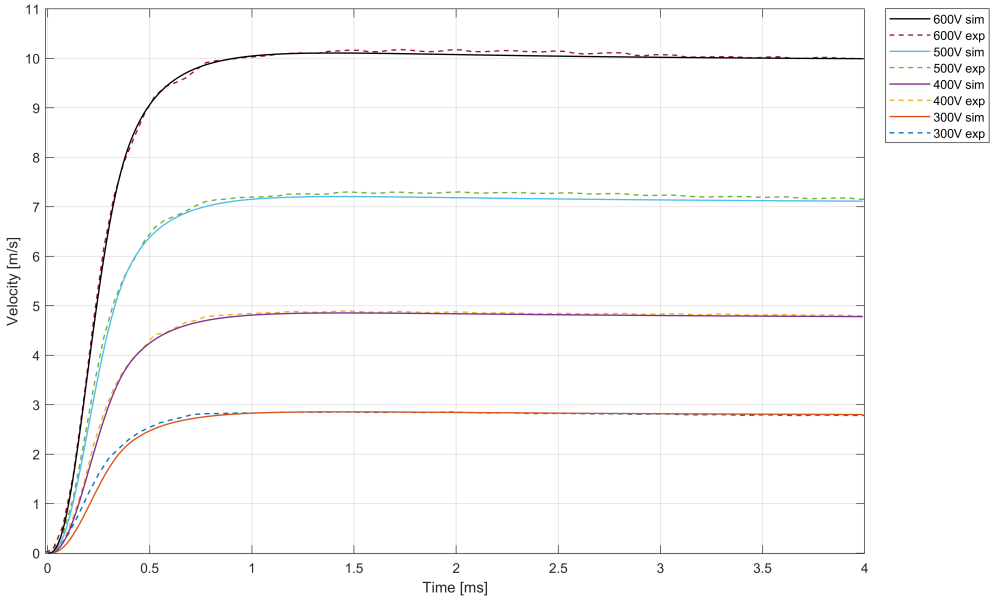

Figure 4.3: A comparison of the armature velocity in the simulation and experiment. The dashed lines represent the experiment and the solid lines represent the simulation.

The largest discrepancy between the simulated and the measured velocity occurs at 300 V, and a closer look at the comparison can be seen in figure 4.4. The discrepancy is not very large and is most obvious during the acceleration phase of the armature. The difference seems to be that the measured velocity starts its acceleration slightly before the simulated velocity. The measured velocity seems to lead the simulated velocity with about 35 μs. The velocity curve shape itself is quite similar, as well as the peak speed. The cause of the discrepancy is hard to pinpoint. It could be a measuring problem, causing a slightly early triggering point, or an inaccuracy in the model, causing a slower initial acceleration. However, looking at the results at the other voltage levels, no such discrepancies are found, indicating that the model is accurate.

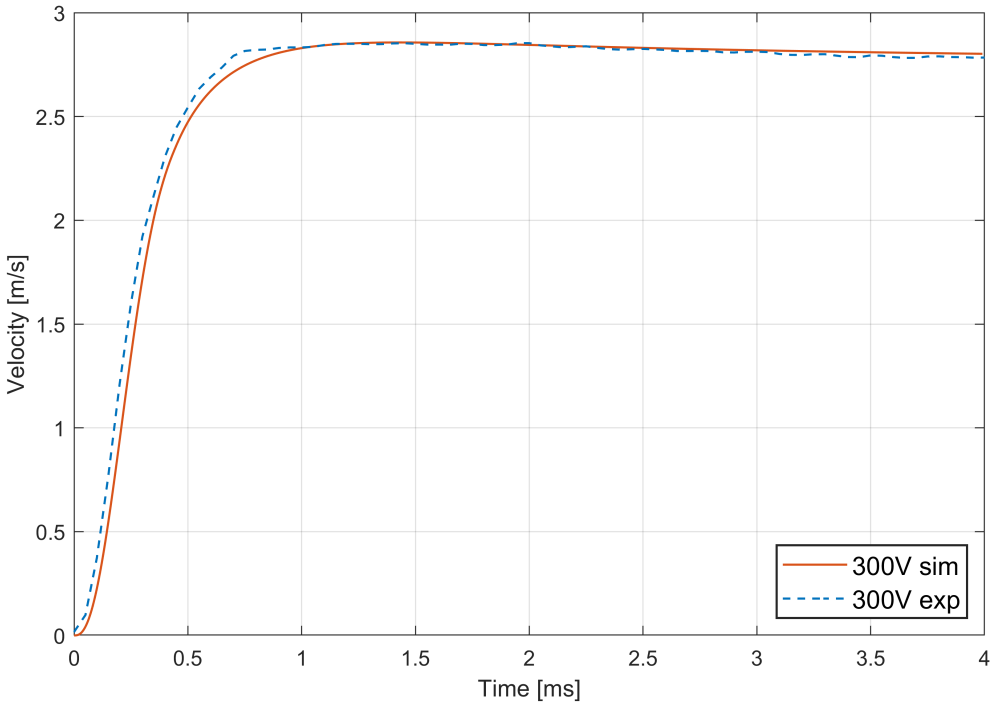

Figure 4.4: A comparison of the armature velocity at 300V, showing a small discrepancy between the simulated and measured velocity.

4.1.2 Capacitor voltage

Figure 4.5 and figure 4.6 show a comparison of the measured capacitor voltage obtained from the experiments and the simulated capacitor voltages. The dashed lines represent the simulated capacitor voltage, and the solid lines represent the measured capacitor voltage. The measured voltage curves coincide very well with the simulated voltage curves. The simulated voltage is slightly higher along the whole curve for all voltage levels. The difference is only 6 V at the maximum in all cases and is constant along the curve until the voltage approaches zero. When the voltage is approaching zero, the voltage difference decreases until reaching zero, where they cross almost at the same time, indicating that the simulated voltage frequency and the measured are equal.

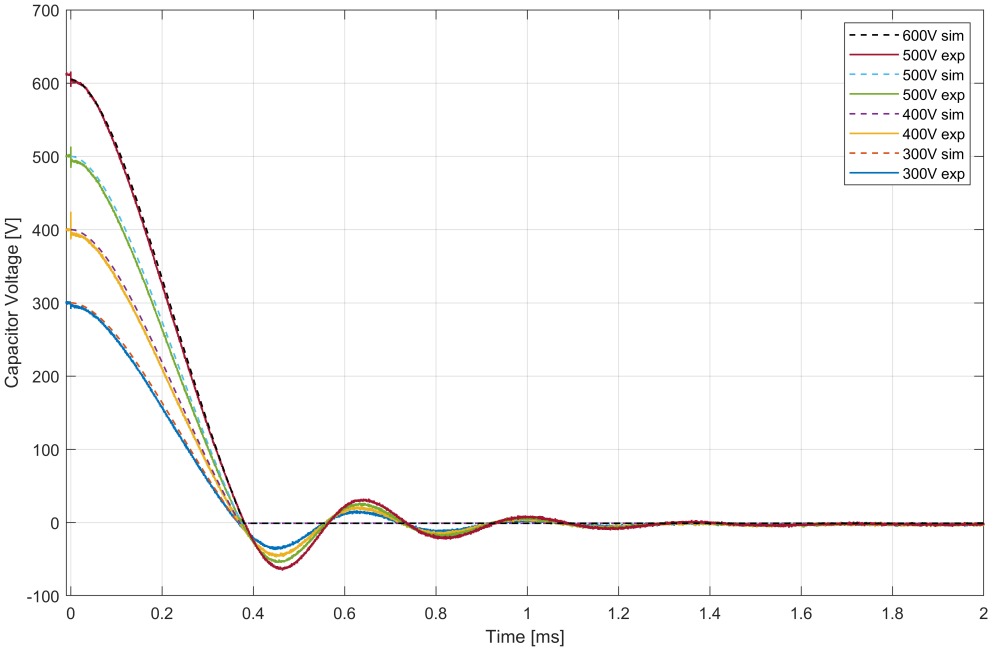

Figure 4.5: A comparison of the simulated and measured capacitor voltage.

At about 0.38 *ms*, the capacitor voltage reaches zero. However, it does not stay at zero. Instead, it continues to a negative value and oscillates back and forth until completely dampened. This shows a negative voltage across the capacitor, indicating that the free-wheeling diode is not conducting. Yet, when looking at the coil current in figure 4.7, the current is always positive, meaning that the diode must be conducting after the voltage reaches zero. The reason why a negative voltage is observed may be because of the grounding of the measuring equipment. The prototype is grounded through the lab's earth ground, and the measuring equipment and voltage probe are isolated with an isolating transformer, separating the grounding points galvanically.

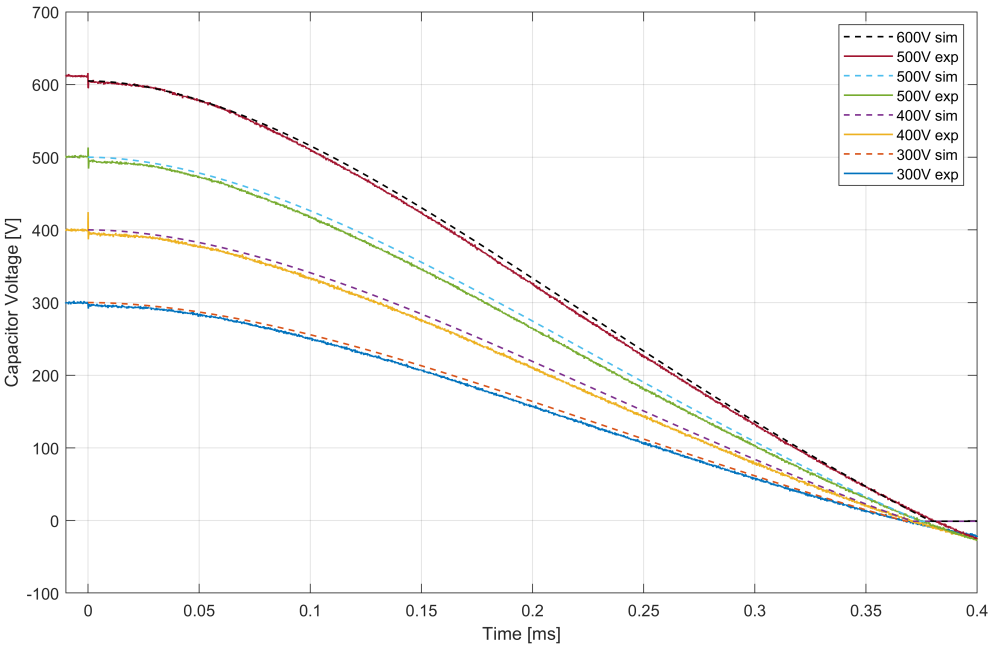

Figure 4.6: A comparison of the simulated and measured capacitor voltage between 0 and 0.4 ms.

4.1.3 Current

In figure 4.7, a comparison of the measured coil currents obtained from the experiment and the simulated coil currents for the different voltage levels are presented. The dashed lines represent the simulated coil current, and the solid lines represent the measured coil current.

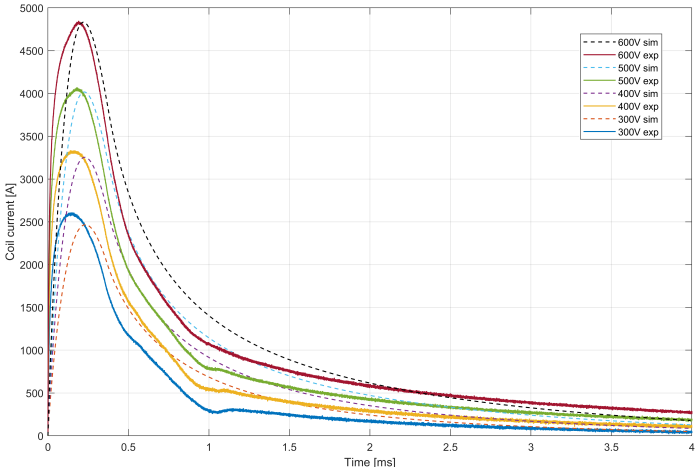

Figure 4.7: A comparison of the simulated and measured coil current from the experiments. Showing the discrepancy between the simulation and experiment.

As seen in the figure, the simulated current curves do not coincide very well with the measured current. The maximum current peaks are similar, especially at the voltage levels of 600 V and 500 V, but at 300 V, a clear difference in the current peak as well. The largest discrepancy between the measured current and the simulated current is the rise time of the currents. The measured coil currents rise extremely fast. The measured coil current has reached approximately 3500 A when at the same time the simulated current has only reached 1500 A, meaning that the measured current reaches 70% of its peak current in the same time that the simulated current only has reached 30% of its peak current. With this large difference in current rise time, a difference in the acceleration between the simulated and the measured velocities should be expected. However, this is not the case. The velocity curves coincide very well for all the cases, indicating that the acceleration of the simulation and experimental measurements are the same. The simulated and measured capacitor voltage also coincide, indicating that the simulated inductance, capacitance and resistance of the system are similar to the actual system that is measured. The measured coil current contradicts the two other measured and simulated parameters, indicating that the discrepancy may come from the measuring method of the current. The measuring method used for measuring the coil current in this experiment was a low-ohmic shunt-resistor in series with the coil. In the article “Using a Current Shunt for the Purpose of High-Current Pulse Measurement” by Piekielny and Waindok they conclude with the following statement: “For a high-current pulse measurement (some kA) there

are very significant differences between current waveforms obtained from a shunt and visible Rogowski coil. The proper current wave is measured by the Rogowski coil, while the shunt does not give the correct result." [27]. In the article, a comparison of the current waves obtained from a Rogowski coil and a current shunt is shown. A mathematical model of the current and the measured current with the Rogowski coil coincide, and it is therefore assumed that the Rogowski coil measures the real current. The comparison of the current waves in the article is very similar to the one observed in figure 4.7. The current steps that occur in the beginning are explained by an induced voltage due to the parasitic inductance of the shunt. Although the inductance is relatively small, for high-current pulses, the results are influenced considerably. As the induced emf on the shunt does not cause any current to flow in the circuit, the peaks are not visible in the Rogowski coil measurements [27]. To further verify the model, the same experiments could be done using a Rogowski coil to measure the coil current instead of the shunt-resistor.

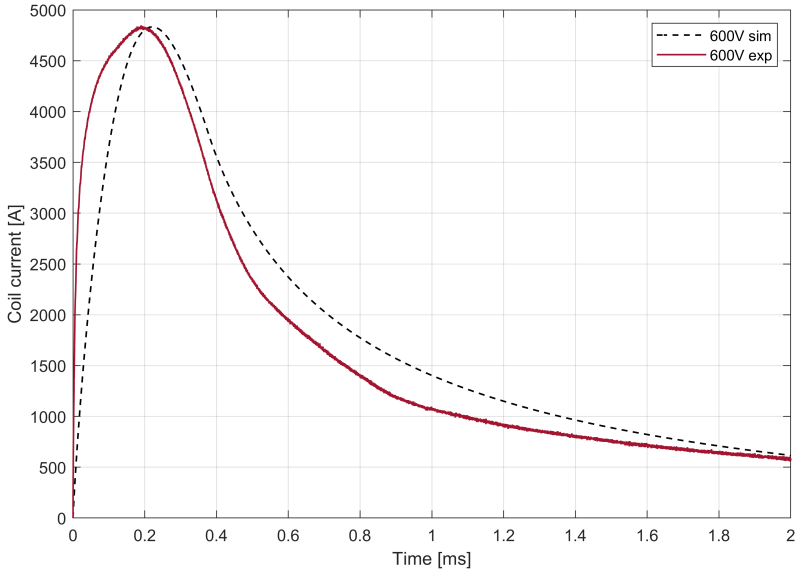

Figure 4.8: A comparison of the simulated and measured coil current at 600V

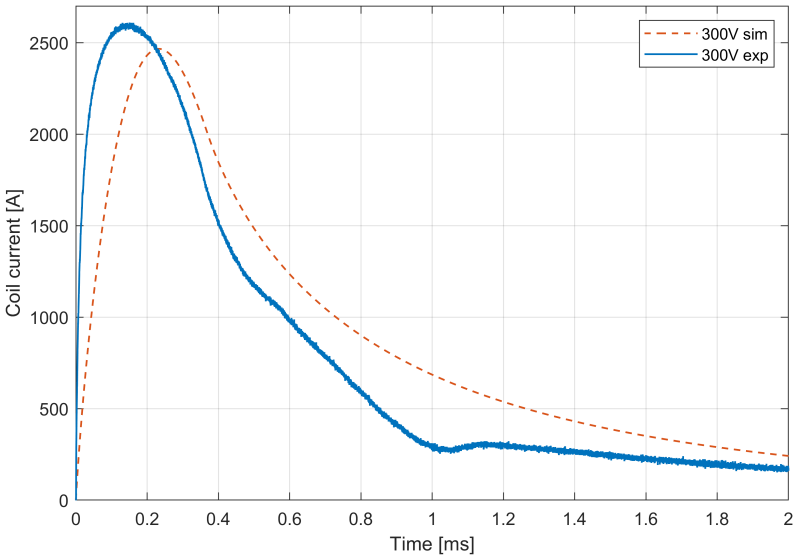

Figure 4.9: A comparison of the simulated and measured coil current at 300V, showing the larges discrepancy between the simulated and measured coil current.

4.2 Parametric study

4.2.1 Energy source - capacitor

Table 4.1 shows all the metrics considered in the results from the ten different simulations for the parametric study of the capacitor.

Table 4.1: The efficiency, opening time and frequency for the different capacitor configurations in the study.

Vol. [V]	Cap. [mF]	E_{el}[J]	Eff. [%]	OT [μs]	Freq. [Hz]
1200	0.694	500	18.57	1959	3205
1100	0.826	500	18.72	1959	2976
1000	1.00	500	18.84	1963	2688
900	1.23	500	18.91	1971	2451
800	1.56	500	18.89	1987	2174
700	2.04	500	18.74	2014	1923
600	2.78	500	18.36	2058	1656
500	4.00	500	17.60	2133	1389
400	6.25	500	16.25	2263	1116
300	11.1	500	13.85	2510	847.5

Figure 4.10 shows a plot of the opening time (OT) in the parameter study. The OT drastically decrease with the change in capacitance and voltage. It is clear that a lower capacitance and higher voltage reduce the OT significantly. However, the reduction in OT starts to decrease towards 900 V and beyond, and from 1100 V to 1200 V, no change in OT is observed. Figure 4.11 shows a plot of the change in efficiency. The plot shows a large increase in efficiency from 300 V to 600 V. This is due to the change in current frequency. A slow rising current pulse causes the armature to move significantly before the peak of the current is reached. The larger air gap reduces the magnetic coupling between the armature and coil and reduces the induced armature current during the largest current peak. This lowers the Lorentz forces between the armature and coil, resulting in a lower efficiency. After 600 V, the increase in efficiency starts to slow down, and it peaks at 800 V with 18.91 %. Beyond 800 V, the efficiency begins to decrease slowly. The decrease in efficiency at the higher frequencies is explained by an increase in the high-frequency conductor resistance due to skin effect [18].

Figure 4.12 shows a plot of the change in frequency, and an almost completely linear increase in frequency due to the change in capacitance is observed. The reason behind the linear increase in frequency can be explained by looking at the resonance frequency of the system. The TC can be seen as an RLC-circuit, giving the resonance frequency of the system as:

$$f_{res} = \frac{1}{2\pi\sqrt{LC}} \tag{4.1}$$

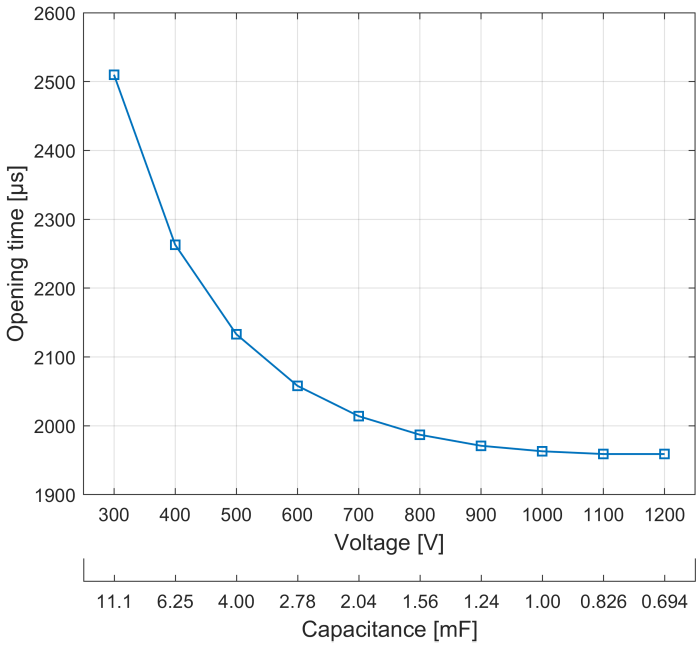

Figure 4.10: The opening time plotted with respect to the change in voltage and capacitance.

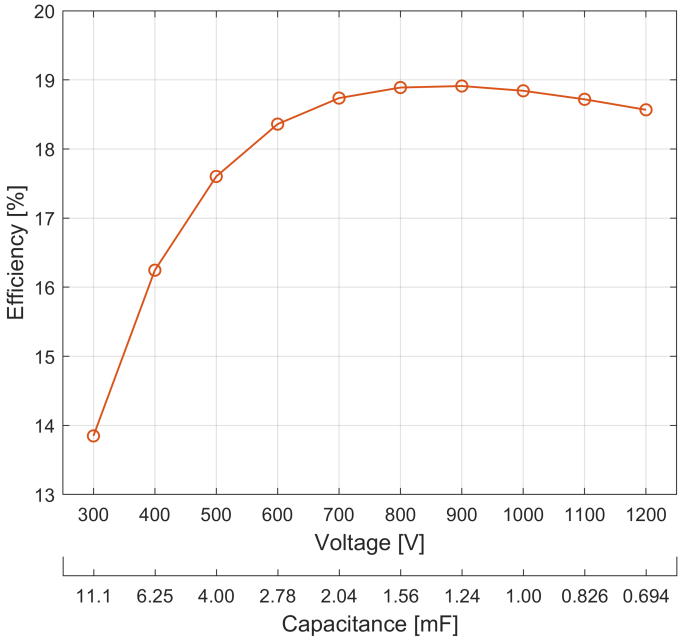

Figure 4.11: The efficiency plotted with respect to the change in voltage and capacitance.

For the parametric study of the capacitor, the inductance of the system L can be

defined as almost constant (The inductance will increase as the armature moves away from the coil, but in this case, the difference between the armature movement for each voltage level is not enough to make significant changes in the inductance for each case), then the inductance can be set as a constant with the other constants:

$$k = \frac{1}{2\pi\sqrt{L}} \tag{4.2}$$

then the resonance frequency can be defined as:

$$f_{res} = k\frac{1}{\sqrt{C}} \tag{4.3}$$

Making the frequency inversely proportional with the square root of the capacitance:

$$f_{res} \propto \frac{1}{\sqrt{C}} \tag{4.4}$$

To keep the energy constant for this case, the square of the capacitance is inversely proportional to the voltages:

$$V_c = \sqrt{\frac{2E}{C}} = \sqrt{2E}\frac{1}{\sqrt{C}} = k\frac{1}{\sqrt{C}} \tag{4.5}$$

As such, the resonance frequency will be proportional to the change in voltage:

$$f_{res} \propto \frac{1}{\sqrt{C}} \propto V_c \tag{4.6}$$

as observed in figure 4.12.

The fastest opening time was at 1200 V, 0.694 mF and 1100 V, 0.826 mF. These voltage levels got the exact same opening time with the same conditions when only changing the capacitor parameters. These levels have relatively high efficiency when compared to the lower voltage levels, and they have the highest current frequencies. The lack of change in OT from 1100 V to 1200 V indicates that the gain in OT from the increased current frequency does not compensate for the lowered efficiency. Making the optimal voltage to capacitance ratio for this system and requirements (50 mm opening distance) somewhere between these two voltage/capacitance levels. This shows that the largest efficiency does not necessarily mean the fastest opening times. However, if the opening distance requirement is increased, a higher correlation between efficiency and OT will be observed due to the greater constant speed obtained at higher efficiencies. The parametric study of the capacitor parameters shows that a high current frequency with relatively high efficiencies will give the fastest opening times.

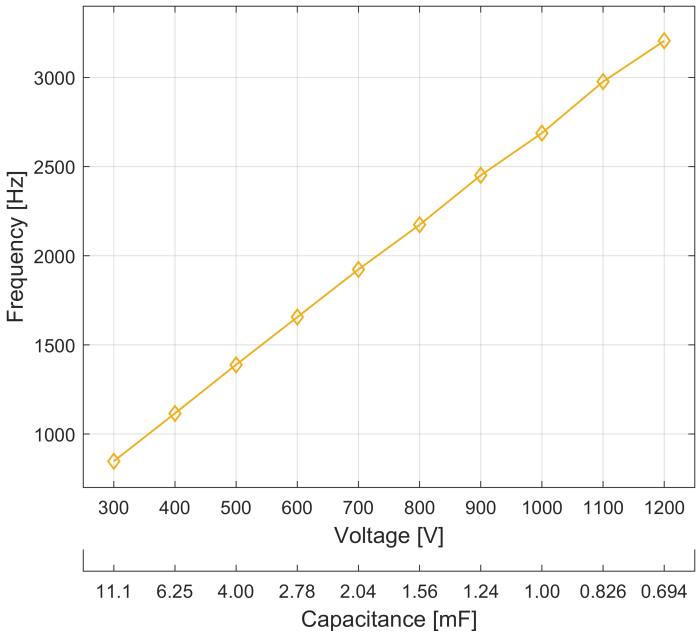

Figure 4.12: The current frequency plotted with respect to the change in voltage and capacitance.

4.2.2 The coil

Table 4.2 shows the results of the parametric study for the number of coil turns.

Table 4.2: The impulse, efficiency, opening time and frequency for the different number of turns in the study.

Turns [N]	Impulse [Ns]	Eff. [%]	OT [μs]	Freq. [Hz]
5	1.211	0.58	10560	7576
10	3.542	5.03	3637	3378
15	5.368	11.65	2470	2252
20	6.412	16.74	2125	1736
25	6.944	19.76	2008	1429
30	7.184	21.26	1977	1225
35	7.254	21.77	1989	1082
40	7.225	21.69	2023	969.0
45	7.136	21.26	2070	883.4
50	7.011	20.61	2126	809.1

Figure 4.13 shows the total current going through the coil for each simulation. The change in turns affects the current waveform significantly when it comes to current peak and frequency. One interesting thing that can be observed is the clear change in inductance as the armature moves away from the coil. This is especially clear from 20 turns and above. The current rises very fast due to the lowered inductance from the presence of the armature. After the current has peaked, the air gap has become large enough to reduce the magnetic coupling between the armature and coil to such an extent that eddy currents in the armature no longer cancel the penetrating magnetic field of the source, thereby increasing the inductance of the system greatly. This is why the slope of the falling current is much less steep.

The magnetic flux density generated by the coil is somewhat proportional to the number of turns and the current flowing in each of the turns (the magnetic field will not be completely uniform, but as a simplification to show a point, the statement is valid). Too few turns do not utilize the coil area efficiently. The coil conductors become too large relative to the current that flows in them, increasing the skin effect and reducing the total coil current that will flow. This is very clear in the case of the coil with five turns. The lowered inductance of a coil with few turns does not compensate for the lowered total current in the coil. As the number of turns increases, the total current also increases, peaking at 15 turns. Figure 4.14 shows the force on the armature in the Z direction. If the force curve is compared to the curve of the total coil current in figure 4.13, a clear relationship between the total coil current and the force can be observed. As the armature moves away, the air gap increases, reducing magnetic coupling, lowering the force on the armature. There is still a significant amount of current flowing in the coil at 1000 μs for the cases with 15 turns and above, but due to the large air gap, almost no force is observed at this point.

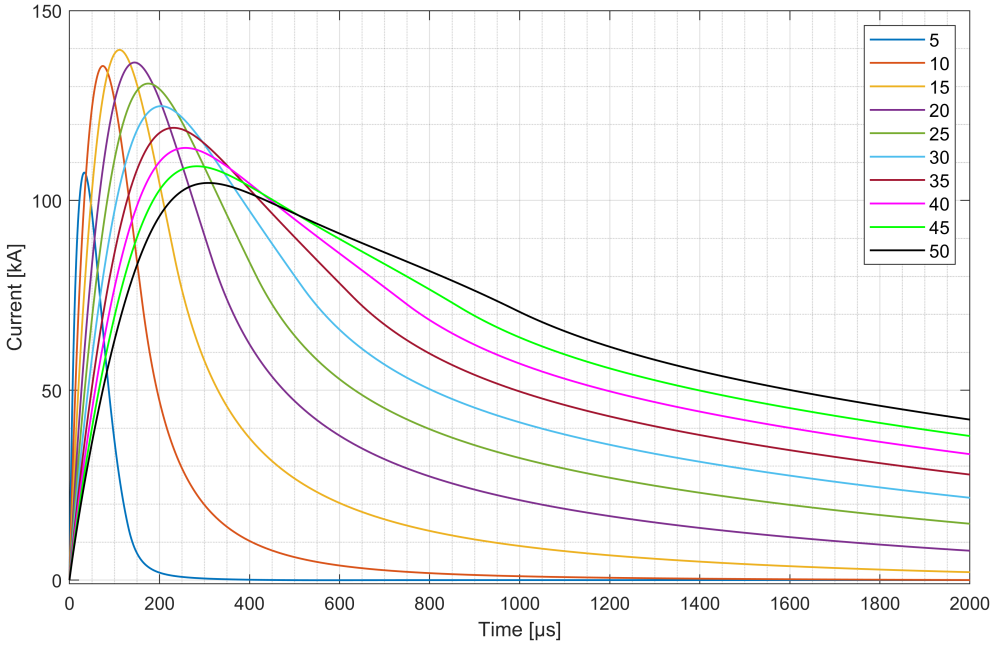

Figure 4.13: The summed coil current of each turn, giving the total current going through the coil.

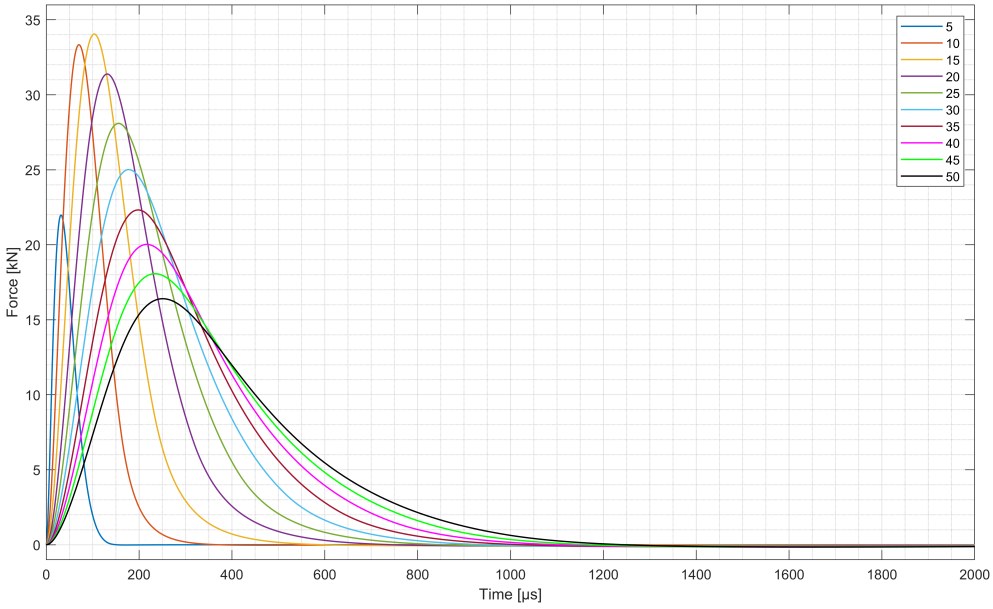

Figure 4.14: The force in the Z direction experienced by the armature.

Not only the magnitude but also the duration of the force is important for fast opening times and high efficiency. The highest peak force happens for the case with 15 turns. However, the duration of the force is significantly shorter than for

the cases with more turns, resulting in a longer OT and lower efficiency. The impulse is the integral of the force, taking into account the duration of the force, making it a better metric of comparison. Figure 4.15 shows a plot of the impulse with respect to the change in the number of turns. It shows a large increase in impulse from 5 to 25 turns, peaking at 35 turns and slightly falling towards 50 turns. Looking at table 4.2 and comparing the efficiency with the impulse, a strong correlation can be observed, rising, peaking and falling similarly. When looking at opening time, the current frequency, as well as the efficiency, plays a role. The fastest opening time is observed at 30 turns with an OT of 1977 μs. However, this is not where the impulse or efficiency is highest. The slightly higher current frequency and peak force gives a faster acceleration earlier but for a shorter amount of time, allowing for the faster opening time even with a lower efficiency when compared to the case with 35 turns. Too few turns result in a low total coil current, giving a high current frequency but a lowered impulse and efficiency. Too many turns reduce the current frequency, slowing down early acceleration and reducing efficiency because of the increased air gap during the largest current peaks. For this case, a combination of high efficiency and high frequency gives the shortest opening times.

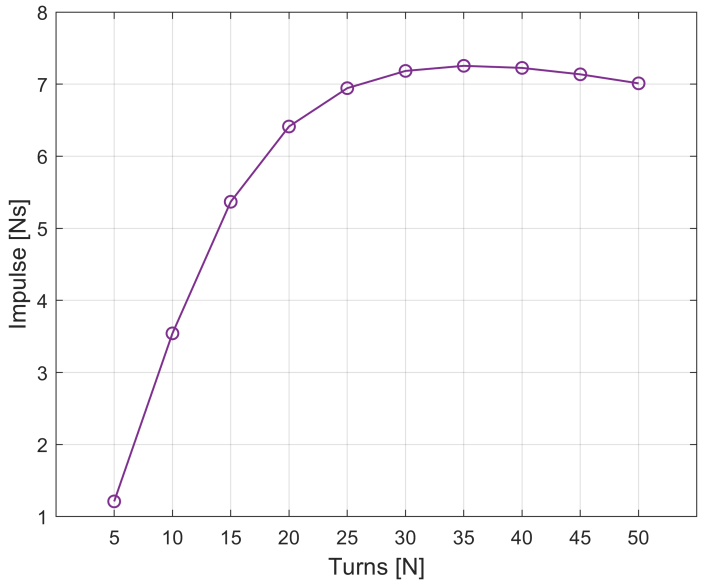

Figure 4.15: The impulse in the Z direction experienced by the armature, plotted with respect to the change in turns

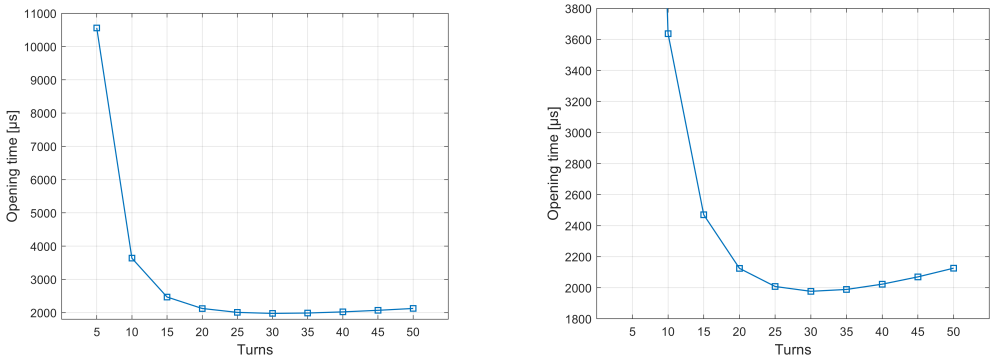

(a) Opening time

(b) A closer look at the opening times between 1800-3800 μs, disregarding the outlier at 5 turns

Figure 4.16: The opening time plotted with respect to the change in turns.

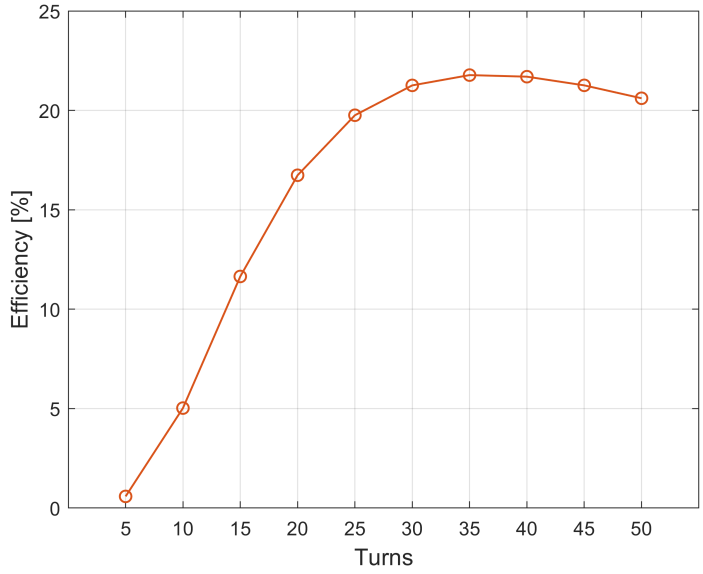

Figure 4.17: The efficiency plotted with respect to the change in turns.

Figure 4.18 shows a plot of the frequency with respect to the change in the number of turns. As the inductance is approximately proportional to the square of the number of turns and the capacitance for this case is constant, the frequency will then be approximately inversely proportional to the number of turns as such:

$$L \propto N^2 \tag{4.7}$$

$$k = \frac{1}{2\pi\sqrt{C}} \tag{4.8}$$

$$f_{res} = \frac{1}{2\pi\sqrt{LC}} = k\frac{1}{\sqrt{L}} \propto \frac{1}{N} \tag{4.9}$$

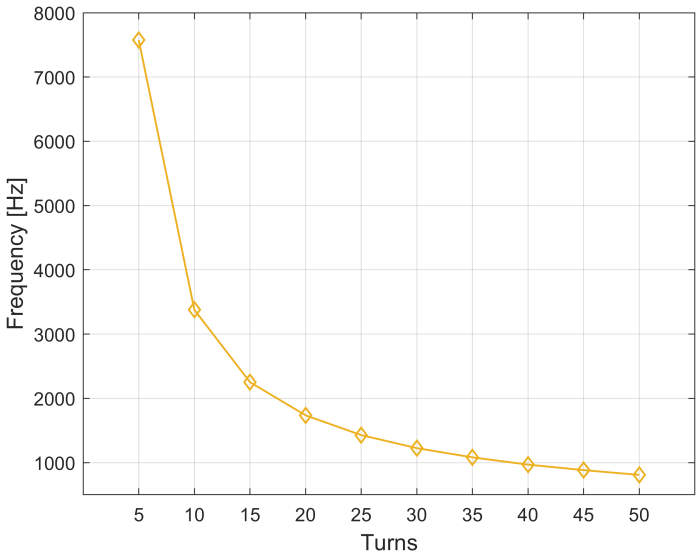

Figure 4.18: The current frequency plotted with respect to the change in turns.

4.2.3 The armature

The change in armature geometry does not change the current frequency significantly and is therefore not investigated for these cases. Instead, the change in armature current, the peak force (F_{peak}), and impulse of the cases are investigated. The values for the peak force and impulse, as well as the armature current are simulated with the armature locked to get an equal basis for comparison for these metrics. When locked, it emphasizes how changes in geometry affect the induced armature current by removing the factor of a change in the air gap. For efficiency and opening time, the armature is allowed to move.

Armature width - change in tolerance

Table 4.3 shows all the metrics considered in the results from the eleven different simulations for the parametric study of the change in tolerance.

Table 4.3: The efficiency, opening time, peak force and impulse for the different tolerances in the study. The values in yellow represents the simulations done with the armature locked in place.

Tol [mm]	M_{arm} [kg]	Eff. [%]	OT [μs]	F_{peak} [kN]	Impulse [Ns]
-10	0.1921	12.92	2072	40.18	7.059
-8	0.2040	13.24	2102	43.21	7.349
-6	0.2164	13.44	2142	45.91	7.599
-4	0.2291	13.50	2192	48.10	7.802
-2	0.2422	13.43	2255	49.63	7.948
0	0.2557	13.20	2333	50.38	8.021
2	0.2697	12.88	2421	50.61	8.050
4	0.2840	12.50	2518	50.61	8.049
6	0.2988	12.13	2618	50.57	8.039
8	0.3140	11.77	2720	50.55	8.032
10	0.3295	10.87	2826	50.53	8.023

The plot of induced armature current in figure 4.19 shows that when the armature radius is smaller than the coil radius, a relatively large portion of the induced armature current is lost. The armature current increases significantly by increasing the radius. The largest increments are gained from -10 mm towards -2 mm, beyond this, the current increase is decaying rapidly, and from 4 mm to 10 mm, the increase is almost negligible.

Figure 4.21 and 4.22 shows the plot of the peak force and impulse respectively. From -10 mm to -2 mm, a significant increase in peak force and impulse can be observed. This is expected because of the significant increase in the armature current observed in the armature current plot. However, at 2 mm and 4 mm, the peak force and impulse reach their maximum value and start to decline slightly with the increase in tolerance, yet the armature current is still increasing. This

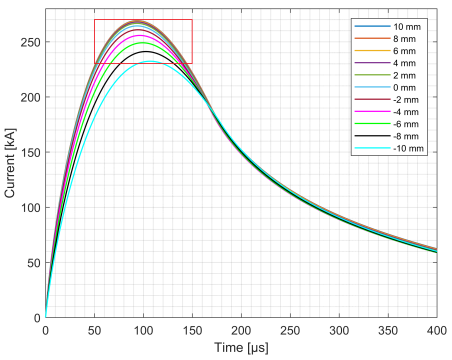

(a) The armature current of each simulation

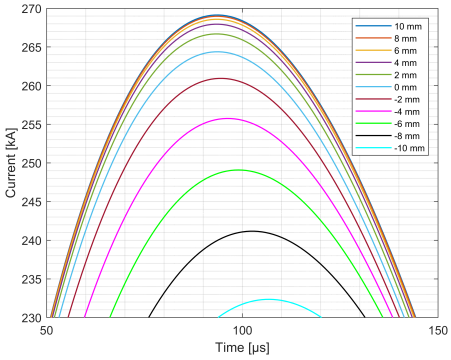

(b) The zoomed in image of the armature current peaks

Figure 4.19: Armature current with the change tolerance as parameter simulated with the armature locked in place.

shows that even with a larger armature current, the armature force is lowered. Intuitively this does not make sense, as the Lorentz force is dependent on the cross product of current density and magnetic flux density: $F = J \times B$. However, even though increasing the armature radius results in an increase in the total current that flows in the armature, it decreases the overall current density in the areas where the magnetic flux density is highest, resulting in a lowered total force applied to the armature. Due to the skin effect, the highest current densities will be near the edges of the armature, which also includes the end edge of the armature, increasing the current density at the end edge. By increasing the armature radius outside the coil radius, the high current density on the end edge is moved out of the area with the largest magnetic flux density, lowering the end edge current density and Lorentz force, as observed in figure 4.20.

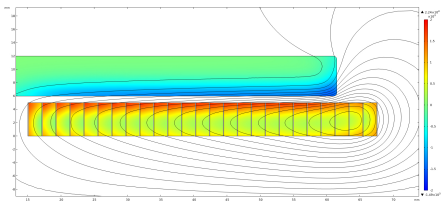

(a) Tolerance set to -6 mm

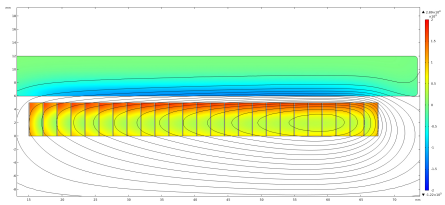

(b) Tolerance set to 6 mm

Figure 4.20: The current density of the armature and coil at 100 μs. The contour lines show the magnetic flux lines.

Looking only at peak force and impulse, having a larger armature radius than the coil radius does not significantly increase the forces between the armature and coil. If anything, the armature radius should be slightly smaller than the radius of the coil.

The efficiency due to the change in tolerance is plotted in figure 4.23. The

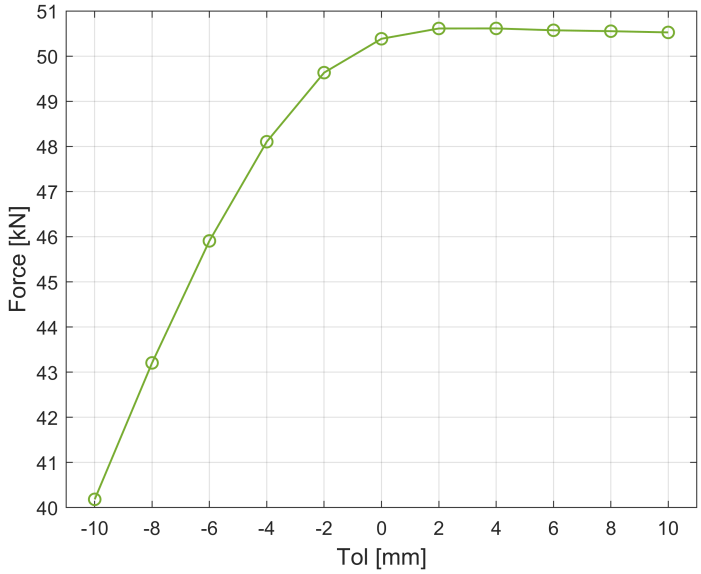

Figure 4.21: Peak force in the Z direction experienced by the armature plotted with respect to change in the tolerance.

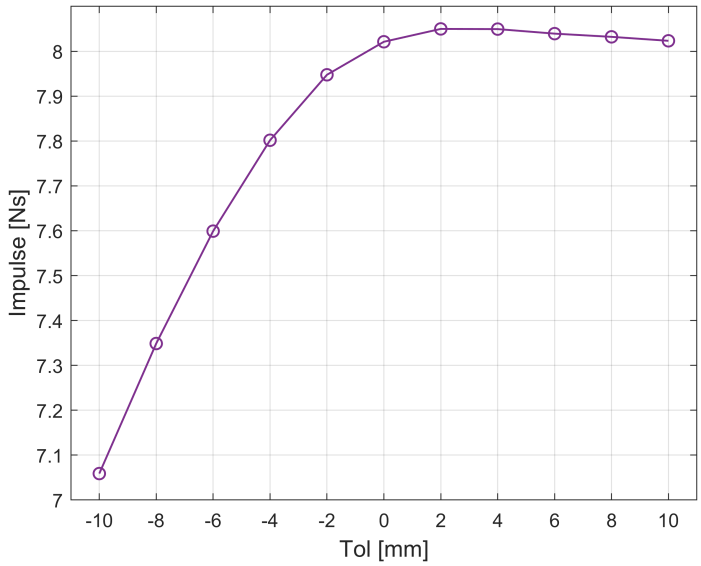

Figure 4.22: Impulse experienced by the armature in the Z direction plotted with respect to change in the tolerance.

efficiency increases with the larger tolerance until a peak is reached at -4 mm. Increasing the tolerance further actually reduces the efficiency almost linearly from 0 mm towards 8 mm and drops even faster towards 10 mm. Increasing the radius without increasing the force significantly just adds unnecessary mass to the armature, reducing its efficiency, whereas letting the radius become too small results in lost armature currents, reducing the efficiency as well.

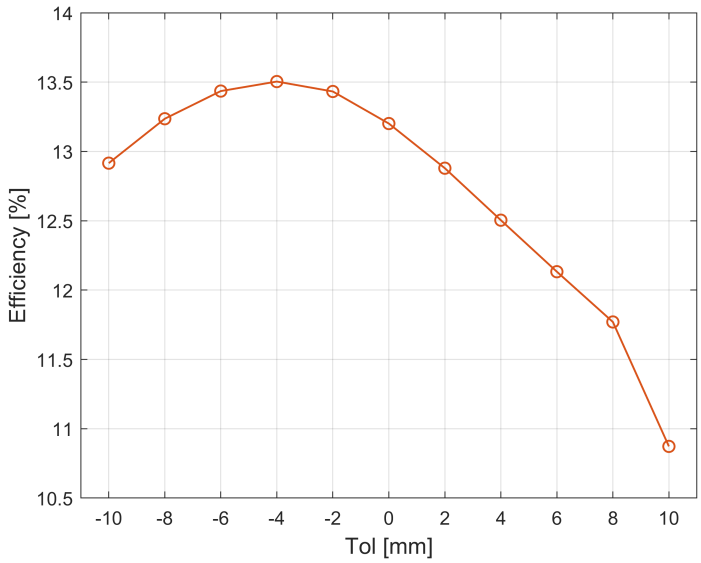

Figure 4.23: The efficiency plotted with respect to change in the tolerance.

Figure 4.24 shows the change in opening time due to the change tolerance. An increase in OT is seen from -10 mm to 10 mm, indicating that the increase in mass does not compensate for the increased force for this case. After 0 mm, a linear increase in OT is observed, showing that no significant increase in force is gained after this. It is important to note that the mass increases proportionally with the square of the radius. If a load was to be moved, the relative mass to the armature must be considered, making efficiency more relevant. I.e. the smaller armature will be more affected by a large increase in mass than the bigger, more massive armature with a higher force and with a slightly higher OT.

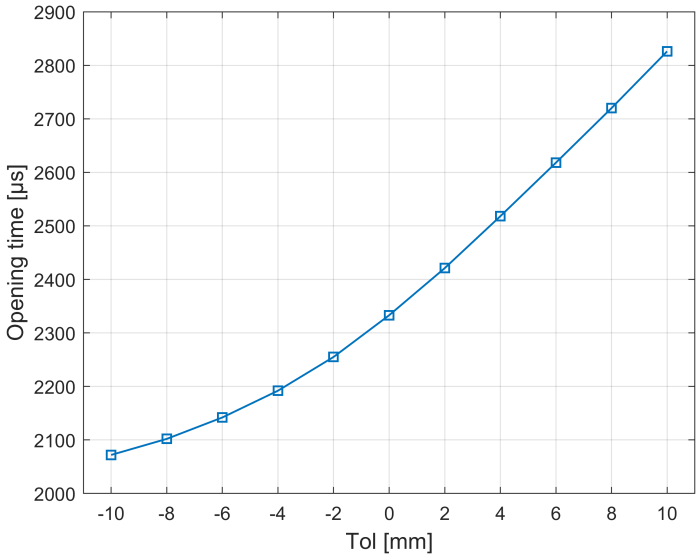

Figure 4.24: The opening time plotted with respect to change in the tolerance.

Armature thickness - change in A_t

Table 4.4 shows the results from the simulations of the ten different armature thicknesses.

Table 4.4: The efficiency, opening time, peak force and impulse for the different thickness levels in the study. The values in yellow represents the simulations done with the armature locked in place.

A_t [mm]	M_{arm} [kg]	Eff. [%]	OT [μs]	F_{peak} [kN]	Impulse [Ns]
22	0.9383	5.85	6522	51.87	8.405
20	0.8551	6.27	6019	51.82	8.393
18	0.7720	6.76	5517	51.75	8.375
16	0.6889	7.33	5013	51.68	8.355
14	0.6057	8.01	4508	51.57	8.330
12	0.5226	8.83	3997	51.45	8.300
10	0.4395	9.84	3487	51.28	8.260
8	0.3564	11.12	2970	51.03	8.193
6	0.2732	12.79	2445	50.63	8.053
4	0.1901	14.88	1915	49.85	7.644

Figure 4.25 shows the induced armature current. A slight increase in armature current can be observed due to the increase in armature thickness. However, the change in armature current is very small, especially for 8 mm and larger, where almost no increase in armature current is observed. This indicates that increasing the armature thickness does not increase the armature current substantially. The skin effect and the exponential decrease in eddy currents with the dept in the material makes the effect of increasing the thickness of the armature inefficient.

The largest difference in armature current can be observed from 4 mm to 6 mm, where a clear dip in the armature current is observed from 200 μs to 600 μs. However, this current dip would not affect the armature force much when it is free to move, as the air gap would have increased significantly.

The small increase in armature current is reflected in the peak force and impulse graphs seen in figure 4.26 and figure 4.27, respectively. From 4 mm to 8 mm, the change in impulse is relatively larger when compared with the change in peak force. This is due to the dip in current between 200-600 μs, which affects the total impulse but not the peak force.

The efficiency seen in figure 4.28 and the OT seen figure 4.29 reflect the insignificant increase in armature current and force. The mass increases linearly with the thickness of the armature without any significant change in force, resulting in a linear increase in opening time. Increasing the armature thickness only increases the mass without any significant increase in armature current, generating a more massive armature, reducing the efficiency of the TC greatly.

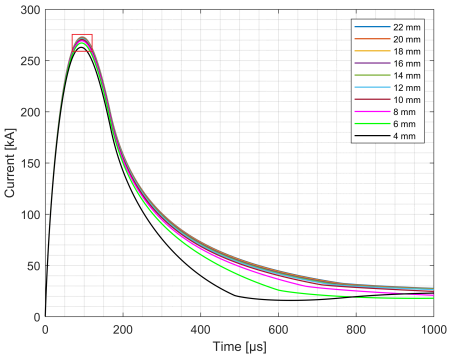

(a) The armature current of each simulation

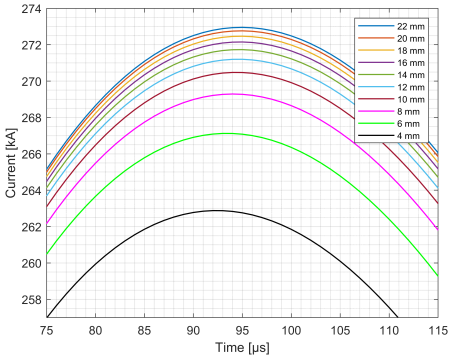

(b) The zoomed in image of the armature current peaks

Figure 4.25: Armature current with the change armature thickness as parameter simulated with the armature locked in place.

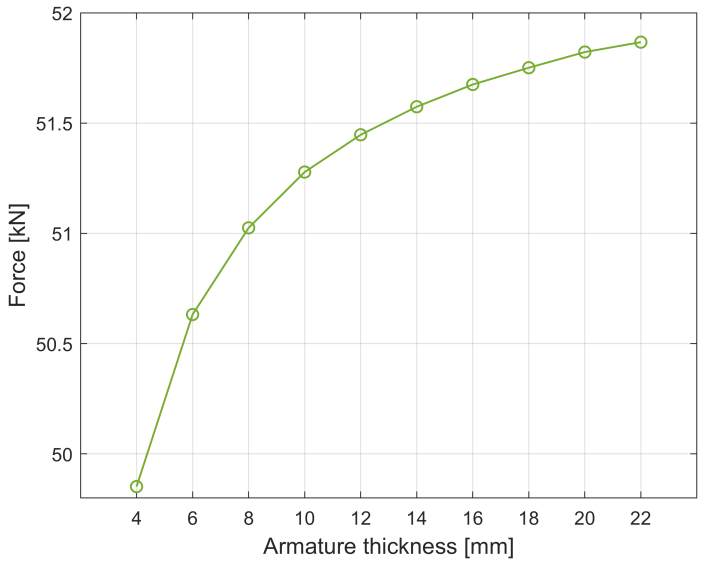

Figure 4.26: Peak force in the Z direction experienced by the armature plotted with respect to change in the armature thickness

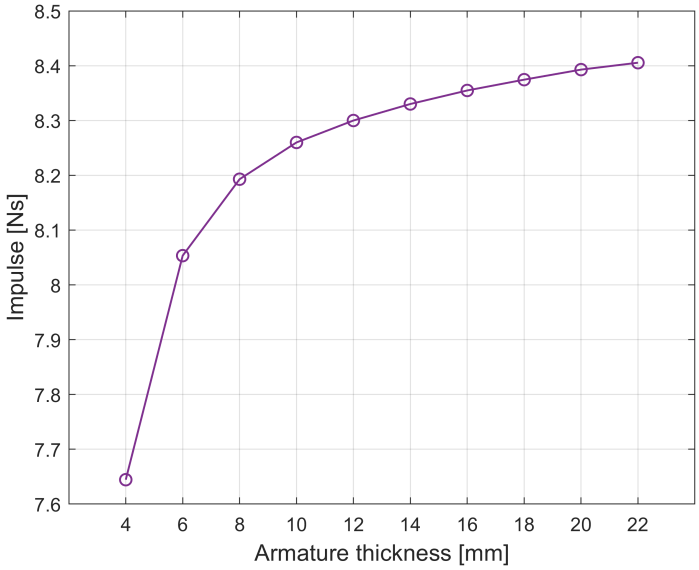

Figure 4.27: Impulse in the Z direction experienced by the armature plotted with respect to change in the armature thickness

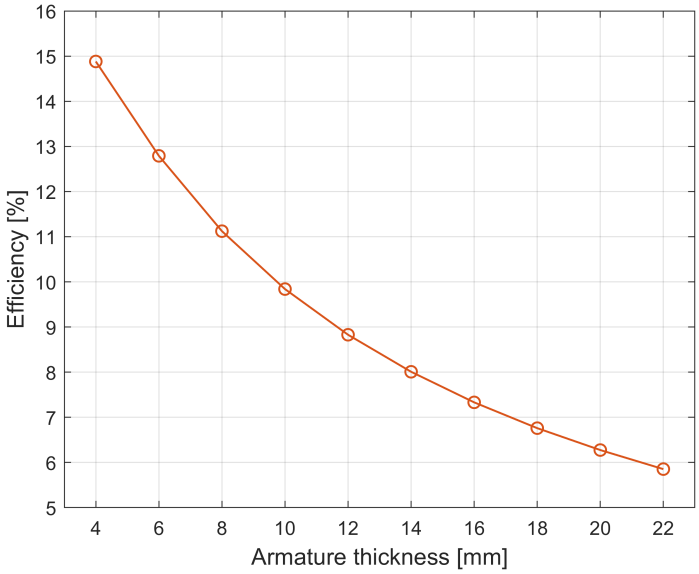

Figure 4.28: Efficiency plotted with respect to change in the armature thickness.

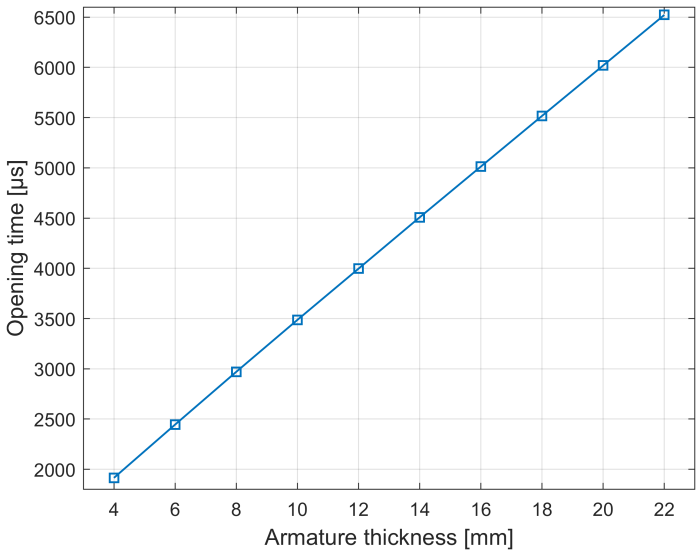

Figure 4.29: Opening time plotted with respect to change in the armature thickness.

Chapter 5

Deriving dimensioning rules for a Thomson coil actuator

The rules presented in this chapter is meant to be a general guideline on how to dimension a TC, and is limited by the parametric study completed in the thesis.

5.1 Iterative design process

Based on the parametric study of the TC some general dimensioning rules can be set for the design of such a device. The thought is that there are two ways the TC can be as a drive mechanism in a circuit breaker. One, the armature is connected to a push/pull rod, driving a load, in this case the current carrying contacts of a hybrid HVDC-DC CB. This means that the armature can be design with only opening time in mind as the armature will not carry any current other than the eddy currents that is induced during opening and closing. Two, the armature is used as the current carrying contacts in the CB. The armature must be designed dependent on the ratings of the CBs as well as opening mechanism. The extra mass in from the push/pull rod and current carrying contacts is removed but the armature needs to be able to carry the rated current of the CBs, potentially increasing the mass of the armature. The iterative design process is divided into the three main components of the TC, the capacitor, the coil and the armature. Even though the process is divided into its respective components, the process is set up in such a way that the component design affects each other, requiring a new iteration of one component when another is changed.

5.1.1 General rules from the parametric study

Some generalized rules or guidelines for the TC design can be set based on the parametric study. For the capacitor: a relatively low capacitance with a high voltage would give the fastest opening times. The lowered capacitance allows for a higher inductance in the coil, increasing the number of turns in the coil. For the coil: a relatively high number of turns (35-45) increases the coil inductance, increasing

the magnetic field from the coil, thus increasing the eddy currents in the armature. For the armature: The armature thickness can be very thin as very little increase in armature current was observed when increasing the thickness of the armature. Most likely, the thickness will be limited by stress more than anything. The armature width should be equal to or slightly smaller (5-6 %) than the coil radius.

5.1.2 Capacitor design

The capacitor can be adapted to fit the design of the armature and coil. The geometry of the capacitor does not affect the design of the armature and coil. As such, it can be adapted to the system's requirements within the design limits of a capacitor. Figure 5.1 shows a flow chart on the iterative design process for the capacitor. The capacitor is sized dependent on the input requirements of the system and the resulting armature mass. From this, an approximated input energy can be calculated. A starting point for the armature and the coil is required to start the process, as well as an assumed efficiency. The assumed efficiency can be set to 15 %, as the parametric study shows this an achievable efficiency with little optimization. The required armature speed should be increased slightly, as it disregards the acceleration phase of the TC. 10 % is a reasonable value as the acceleration phase last about 10 % of armatures movement time for the cases with reasonable opening time in the parametric study. The parametric study indicates that having a relatively low capacitance while compensating with a higher voltage would result in faster OT. This suggests that starting the iterative process at a high voltage can be advantageous. The simulation results can then be used to optimize the capacitor's voltage/capacitance ratio, and the efficiency and speed requirements can be adjusted for the next iteration.

5.1.3 Coil design

Excessive temperature in the coil may damage the enamel [28]. As such, a limit to the maximum allowed change in temperature needs to be set. If it is assumed that all the energy is dissipated in the coil, the calculated heat change can be calculated by the following equation:

$$\Delta T = \frac{C \cdot V_c^2}{2 \cdot m_{coil} \cdot c_p} \tag{5.1}$$

Where C represents the capacitance of the capacitor, V_c is the capacitor voltage, m_{coil} is the mass of the conducting material in the coil, and c_p is the heat capacity of copper. By setting a maximum allowed change in the temperature per switching, the required mass of the material can be calculated. Figure 5.2 shows the flow chart for the coil design, and the coil radius can be calculated from following equation [24]:

$$C_r = C_{ir} + N \cdot C_w + 2 \cdot (N-1) \cdot e_w \tag{5.2}$$

and is implemented in the flow chart. To get a starting point for the iterative process, a conductor width must be chosen, as well as the inner radius, and a starting

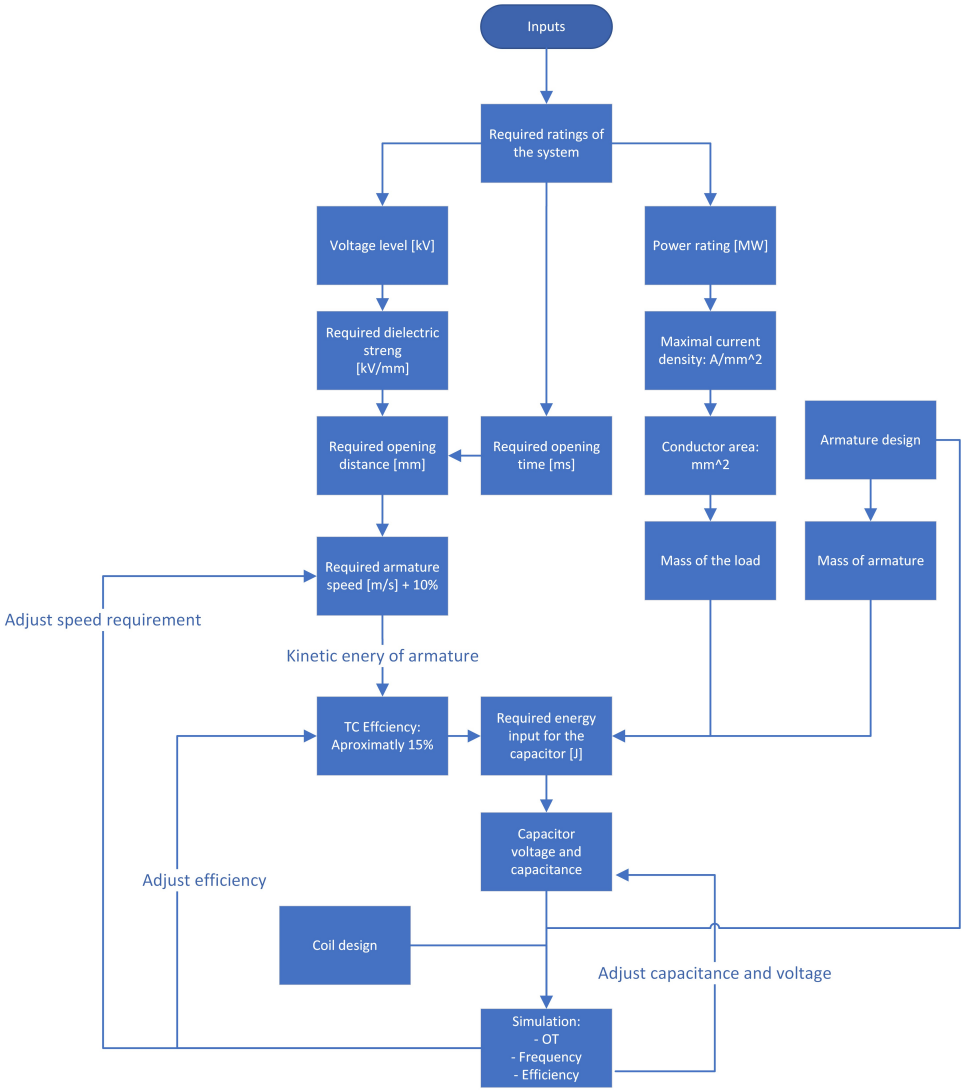

Figure 5.1: Flow chart of the iterative design process of the capacitor.

point for the coil turns. The conductor width could be based on a standardized magnet wire with a rectangular shape. The starting point for the turns is based on the parametric study and can be set to 35. The required energy input will limit the current density in the wire by increasing the conductor height (If the height-to-width ratio of the conductor becomes very high, a constraint could be added). The armature radius will change depending on the coil radius, causing the mass to change, in turn changing the required energy input. With the first iteration of the armature design ready, the iterative design process of the coil can continue until a satisfactory opening time is achieved.

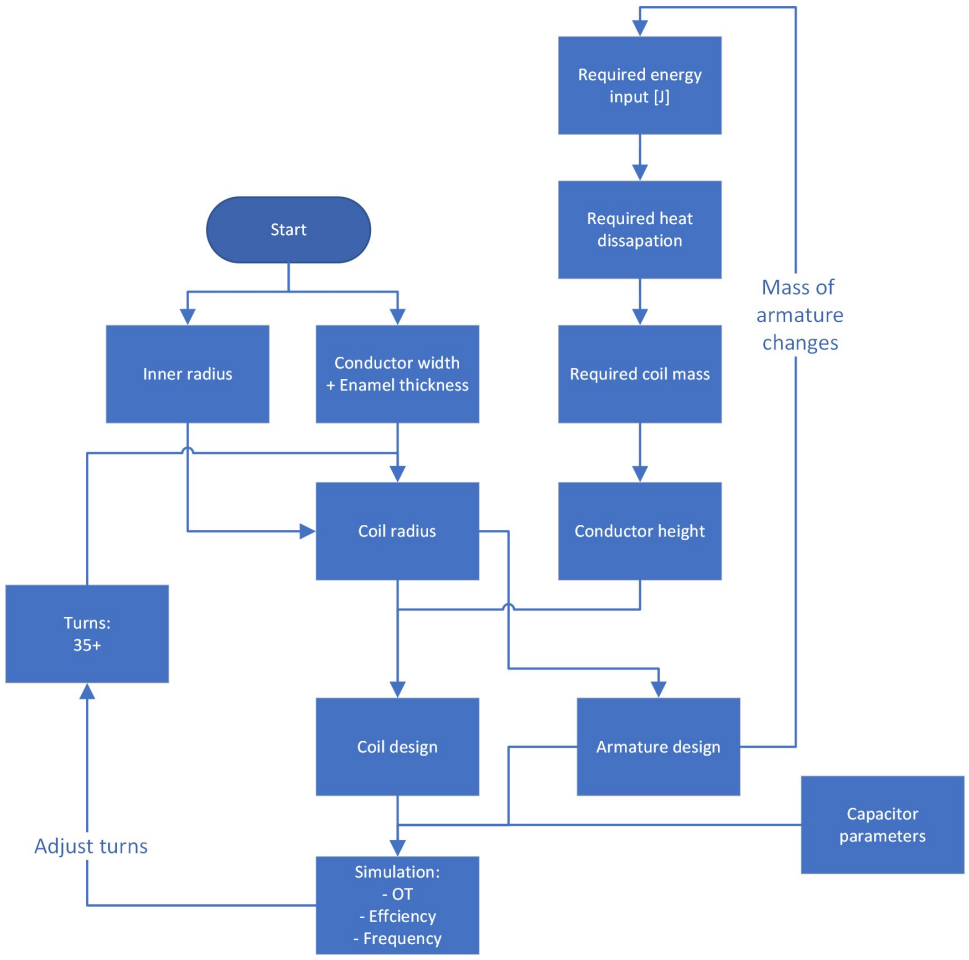

Figure 5.2: Flow chart of the iterative design process of the coil.

5.1.4 Armature design

To limit the design parameters, the armature radius is based on the coil radius. (Based on the parametric study, it was shown that the improvement from optimization of the armature was minimal, just minimizing the mass of the armature would increase the efficiency the most.) The limitation of the armature design differs depending on if the armature will be used as a current-carrying contact or just drive a load mass. Figure 5.3 shows the flow chart depending on the armature type. Based on the parametric study of the armature width the armature radius is set slightly smaller than the coil radius (5-6 % smaller gave the highest efficiency). The armature thickness is set to be as thin as possible within the limitations of the penetration dept of eddy currents and force stress that the armature can handle without permanently deforming [18]. The parametric study shows even for very thin armatures (4 mm), the increase in thickness did not significantly increase the

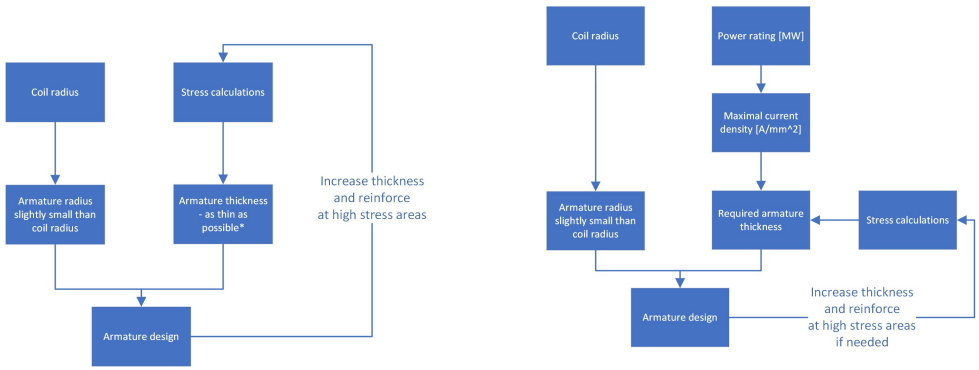

(a) Load driving armature **(b)** Current carrying armature

Figure 5.3: Flow chart of the iterative design of the armature.

armature current. As such, the limiting factor of the armature thickness would most likely be the stress forces on the armature during opening. By implementing solid mechanics in the simulation model, the mechanical stress can be calculated [29], and from that the required armature thickness can be set. For the current-carrying armature, the required initial armature thickness is set from the required power rating and from that, a stress calculation is done to check if the armature design can handle the stress forces.

Chapter 6

Conclusion and future work

6.1 Conclusion

The experimental verification of the general concepts behind the simulation model was confirmed within the limitation of the model. The model was verified at all voltage levels with good accuracy, indicating that the model design is adaptable and robust. However, the assumption that the armature is infinitely stiff may not be valid for less robust armatures. The armature in the prototype was overdimensioned, making it very stiff, making the model valid for this case.

The parametric study shows some clear tendencies when it comes to optimization of efficiency and opening time for the different components allowing for some conclusions about the factors that affect the driving characteristics of the Thomson coil actuator: For any given TC, there would be an optimal energy source with regard to opening time and energy input. This means that if the energy input is limited to a maximum constant energy and the voltage and capacitance are varied with respect to each other, for that given energy and TC, an optimal voltage to capacitance ratio can be found, making the capacitor the easiest component to adapt to the system. For the coil, a relatively high number of turns (35-45) allows for a larger magnetic field, thus increasing the eddy currents in the armature. However, the increased inductance reduces the currents rise rate, reducing the initial acceleration. Consequently, an optimization of the coil is required to find the fastest OT for the specific case. The armature radius should be equal to or slightly smaller than the coil radius. Increasing the armature thickness did not affect the armature current significantly, making it likely that the limiting factor of the armature thickness and design will be the force stress.

Making generalized dimensioning rules for a Thomson coil actuator is challenging due to the many factor and parameters that affect the driving characteristics of the device. The design and optimization of electromagnetic devices have historically shown to be a complex and time-consuming task, and still is. The implementation of FEM-simulation models allows for faster and more cost-effective exploration of the design parameters. The iterative design process suggested in the thesis requires the implementation of stress calculations in the model before it can

be tested. Even with the limitations set for the design process, the flow charts for the iterative design process become complex and intricate, highlighting the difficulty of making general dimensioning rules for such devices. Standardizing the mechanism for different voltage levels and power ratings might be possible but require specific design and optimization within the limits of the requirements for the specific system.

6.2 Future work

- Remeasure the coil current of the prototype with a Rogowski coil and compare the results with the shunt measurements.
- Implementing solid mechanics in the model to calculate the armature stress and to further improve the fidelity of the model.
- Test the suggested iterative design process.
- Expand the parametric study to include more parameters.
- Make a prototype of a TC with a current-carrying armature.
- Standardize the sizing of a TC for specific system ratings.

Bibliography

[1] H. R. Hansen, *Simulation and design of an electrodynamic thomson coil actuator for fast mechanical switches*, NTNU, 2022.

[2] 'The paris agreement.' https://unfccc.int/process-and-meetings/the-paris-agreement/the-paris-agreement. (2022). (accessed: 05.01.2022).

[3] A. Bissal, 'Modeling and verification of ultra-fast electro-mechanical actuators for hvdc breakers,' Ph.D. dissertation, KTH Royal Institute of Technology, 2015.

[4] C. Meyer, M. Kowal and R. De Doncker, 'Circuit breaker concepts for future high-power dc-applications,' in *Fourtieth IAS Annual Meeting. Conference Record of the 2005 Industry Applications Conference, 2005.*, vol. 2, 2005, 860–866 Vol. 2. DOI: 10.1109/IAS.2005.1518439.

[5] F. Mohammadi, K. Rouzbehi, M. Hajian, K. Niayesh, G. B. Gharehpetian, H. Saad, M. Hasan Ali and V. K. Sood, 'Hvdc circuit breakers: A comprehensive review,' *IEEE Transactions on Power Electronics*, vol. 36, no. 12, pp. 13 726–13 739, 2021. DOI: 10.1109/TPEL.2021.3073895.

[6] J. Hafner, 'Proactive hybrid hvdc breakers-a key innovation for reliable hvdc grids,' in *Proc. CIGRE Bologna Symposium*, 2011, pp. 1–8.

[7] M. Callavik, A. Blomberg, J. Häfner and B. Jacobson, 'Break-through!: Abb's hybrid hvdc breaker, an innovation breakthrough enabling reliable hvdc grids,' *Abb Rev*, vol. 2, pp. 7–13, 2013.

[8] E. Ø. Norum, 'Design and operation principles of dc circuit breakers-development of a solid state dc breaker for the ntnu/sintef smart grid and renewable energy laboratory,' M.S. thesis, NTNU, 2016.

[9] Y. Bingjian, G. Yang, W. Xiaoguang, H. Zhiyuan, C. Longlong and S. Yunhai, 'A hybrid circuit breaker for dc-application,' in *2015 IEEE First International Conference on DC Microgrids (ICDCM)*, 2015, pp. 187–192. DOI: 10.1109/ICDCM.2015.7152036.

[10] G. Liu, F. Xu, Z. Xu, Z. Zhang and G. Tang, 'Assembly hvdc breaker for hvdc grids with modular multilevel converters,' *IEEE Transactions on Power Electronics*, vol. 32, no. 2, pp. 931–941, 2017. DOI: 10.1109/TPEL.2016.2540808.

[11] M. Callavik, A. Blomberg, J. Hafner and B. Jacobson, 'Break-through!: Abb's hybrid hvdc breaker, an innovation breakthrough enabling reliable hvdc grids,' *Reseachgate*, 2013.

[12] C. C. Davidson, R. S. Whitehouse, C. D. Barker, J.-P. Dupraz and W. Grieshaber, 'A new ultra-fast hvdc circuit breaker for meshed dc networks,' in *11th IET International Conference on AC and DC Power Transmission*, 2015, pp. 1–7. DOI: 10.1049/cp.2015.0021.

[13] K. Niayesh and M. Runde, *Power Switching Components*. 2017, ISBN: 978-3-319-84656-9.

[14] *Comsol documentation*, English, COMSOL multiphysics, (accessed: dd.mm.yyyy).

[15] M. N. O. Sadiku, *Elements of Electromagnetics*, ser. 4th ed. New York Oxford: Oxford University Press, 2007, ISBN: 978-0-19-530048-2.

[16] *How to create eddy currents*, Picture, https://imamagnets.com/en/blog/eddy-current, 2018, (accessed: 11.01.2022).

[17] R. K. Wangsness and R. K. Wangsness, *Electromagnetic fields*. Wiley New York, 1979, vol. 2.

[18] I. S. University. 'Depth of penetration and current density.' https://www.nde-ed.org/Physics/Electricity/depthcurrentdensity.xhtml. (). (accessed: 19.05.2022).

[19] J. D. Jackson, *Classical electrodynamics*, ser. 3rd ed. Wiley, 1999, ISBN: 0-471-30932-X.

[20] D. J. Griffiths, *Introduction to electrodynamics*, ser. 3rd ed. Prentice Hall, 1999, ISBN: 978-0-13-805326-0.

[21] K. L. Kaiser, *Electromagnetic compatibility handbook*. CRC press, 2004.

[22] C. multiphysics. 'Introduction to field electromagnetics.' https://www.comsol.com/multiphysics/electromagnetics. (2019). (accessed: 11.01.2022).

[23] R. D. Garzon, *High voltage circuit breakers: design and applications*. CRC Press, 2002.

[24] A. Bissal, J. Magnusson, E. Salinas and G. Engdahl, 'Multiphysics modeling and experimental verification of ultra-fast electro-mechanical actuators,' *International Journal of Applied Electromagnetics and Mechanics*, vol. 49, pp. 51–59, Sep. 2015. DOI: 10.3233/JAE-140176.

[25] I. Hussain and D.-K. Woo, 'Self-inductance calculation of the archimedean spiral coil,' *Energies*, vol. 15, no. 1, 2022, ISSN: 1996-1073. DOI: 10.3390/en15010253. [Online]. Available: https://www.mdpi.com/1996-1073/15/1/253.

[26] 'Detectmineigenfeatures.' (2022), [Online]. Available: https://se.mathworks.com/help/vision/ref/detectmineigenfeatures.html#btol2bp-1-points. (accessed: 29.05.2022).

[27] P. Piekielny and A. Waindok, 'Using a current shunt for the purpose of high-current pulse measurement,' *Sensors*, vol. 21, no. 5, p. 1835, 2021.

[28] B. Petitgas, G. Seytre, O. Gain, G. Boiteux, I. Royaud, A. Serghei, A. Gimenez and A. Anton, 'High temperature aging of enameled copper wire — relationships between chemical structure and electrical behavior,' in *2011 Annual Report Conference on Electrical Insulation and Dielectric Phenomena*, 2011, pp. 84–88. DOI: 10.1109/CEIDP.2011.6232602.

[29] M. Al-Dweikat, J. Cui, S. Sun, M. Yang, G. Zhang and Y. Geng, 'A review on thomson coil actuators in fast mechanical switching,' in *Actuators*, Multidisciplinary Digital Publishing Institute, vol. 11, 2022, p. 154.

Appendix A

Prototype schematics

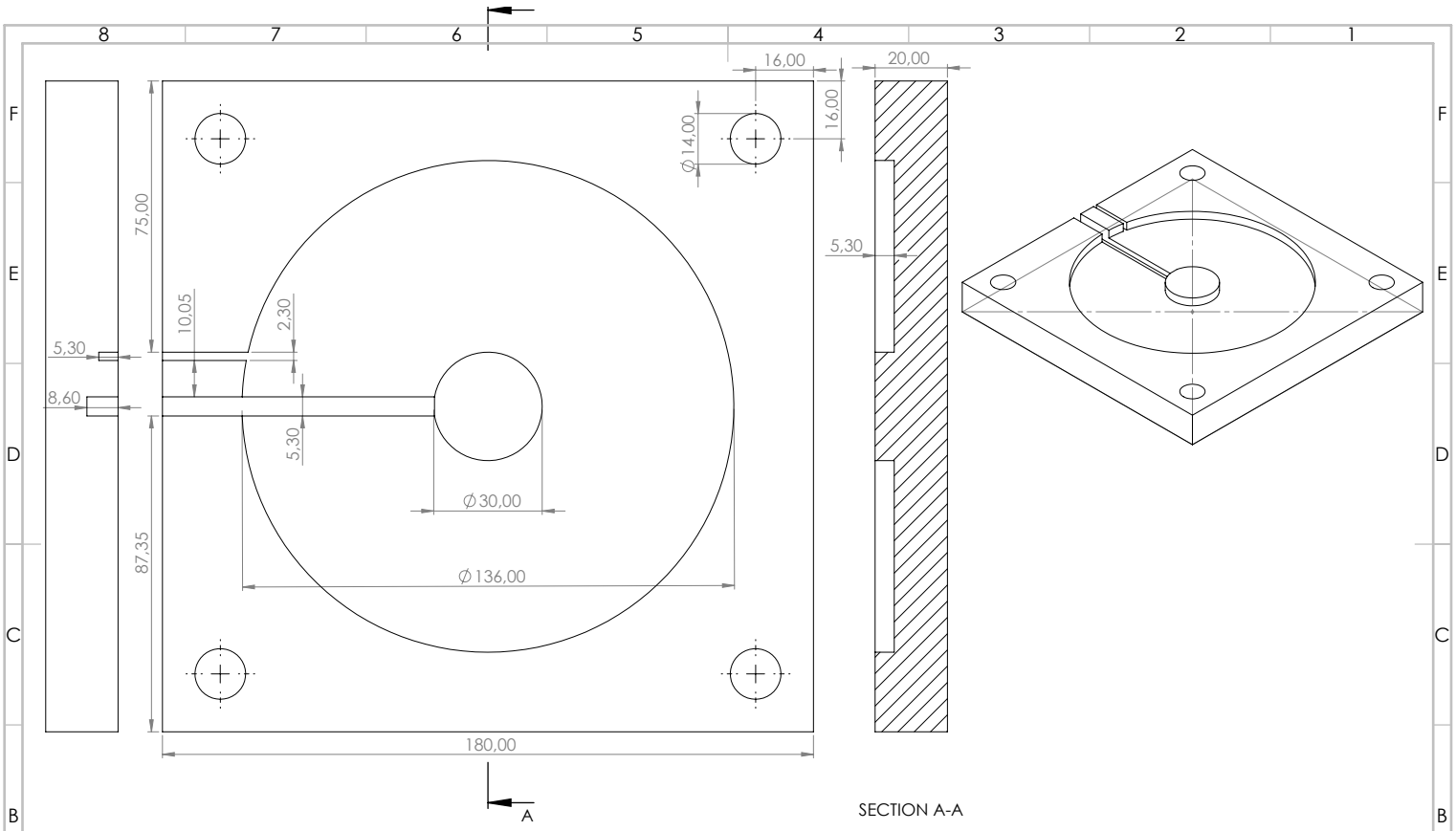

SECTION A-A

UNLESS OTHERWISE SPECIFIED: DIMENSIONS ARE IN MILLIMETERS SURFACE FINISH: TOLERANCES: LINEAR: ANGULAR:		FINISH:				DEBURR AND BREAK SHARP EDGES	DO NOT SCALE DRAWING	REVISION
	NAME	SIGNATURE	DATE				TITLE:	
DRAWN	Håkon R. Hansen		25.02.22					
CHKD								
APPV'D								
MFG								
Q.A				MATERIAL: Pertinax (Synthetic resin bonded paper)			DWG NO. Coil_housing_iteration4	A3
				WEIGHT:			SCALE:1:1	SHEET 1 OF 1

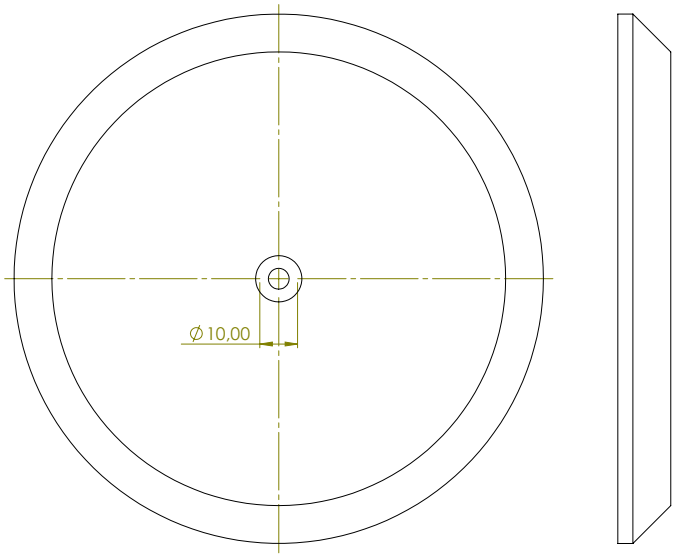

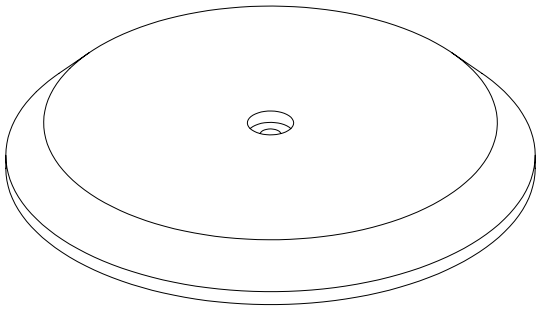

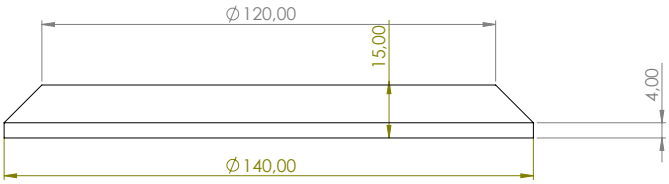

UNLESS OTHERWISE SPECIFIED: DIMENSIONS ARE IN MILLIMETERS SURFACE FINISH: TOLERANCES: LINEAR: ANGULAR:		FINISH:		DEBURR AND BREAK SHARP EDGES		DO NOT SCALE DRAWING	REVISION
	NAME	SIGNATURE	DATE			TITLE:	
DRAWN	Håkon R. Hansen						
CHKD							
APPV'D							
MFG							
Q.A				MATERIAL: Aluminium		DWG NO. Armature 2	A3
				WEIGHT:		SCALE:1:1	SHEET 1 OF 1

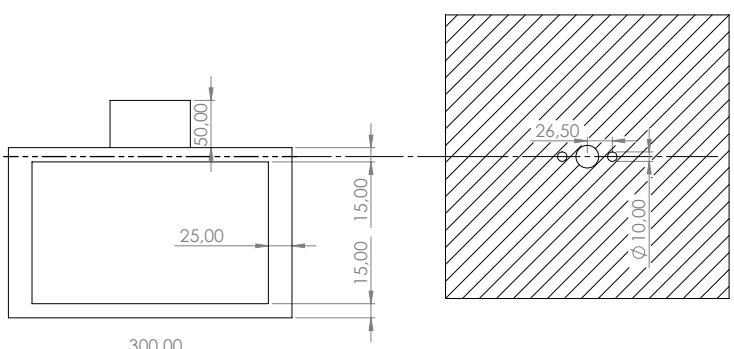

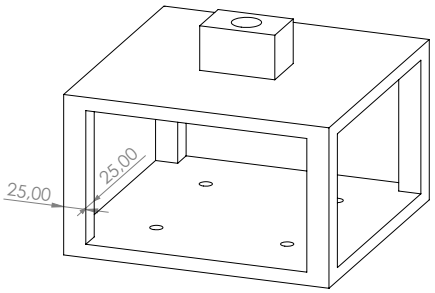

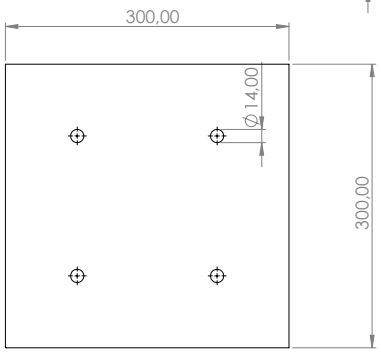

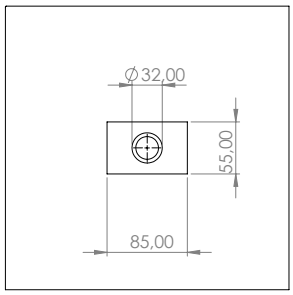

UNLESS OTHERWISE SPECIFIED: DIMENSIONS ARE IN MILLIMETERS SURFACE FINISH: TOLERANCES: LINEAR: ANGULAR:		FINISH:			DEBURR AND BREAK SHARP EDGES	DO NOT SCALE DRAWING	REVISION
	NAME	SIGNATURE	DATE			TITLE:	
DRAWN	Håkon R. Hansen						
CHKD							
APPV'D							
MFG							
Q.A				MATERIAL: Steel		DWG NO. Rack	A3
				WEIGHT:		SCALE:1:4	SHEET 1 OF 1

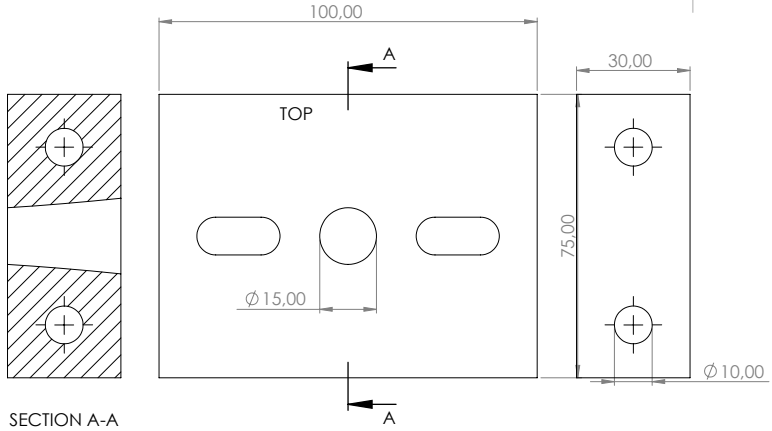

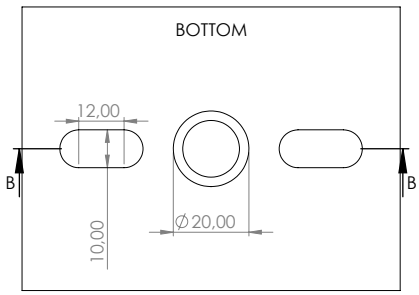

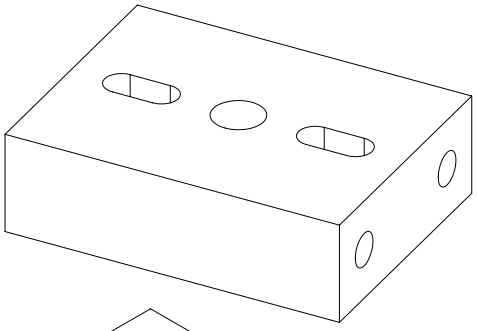

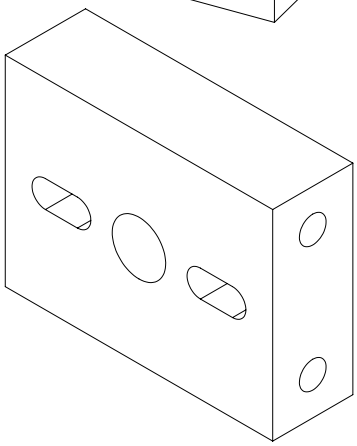

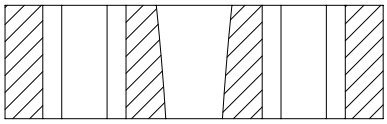

SECTION B-B

UNLESS OTHERWISE SPECIFIED: DIMENSIONS ARE IN MILLIMETERS SURFACE FINISH: TOLERANCES: LINEAR: ANGULAR:		FINISH:			DEBURR AND BREAK SHARP EDGES	DO NOT SCALE DRAWING / REVISION
	NAME	SIGNATURE	DATE			TITLE: Kile for guide rod. Den skal være delt horisontalt, og klemmes sammen. Målet er at styrestangen skal kile seg fast etter at armaturen har blitt avlyst. Deretter kan man løsne stangen ved å skru løs skruene på sidene slik at kilen slipper taket på stangen.
DRAWN	Håkon R. Hansen					
CHKD						
APPV'D						
MFG						
Q.A				MATERIAL: Steel		DWG NO. Rod_wedge — A3
				WEIGHT:		SCALE:1:1 — SHEET 1 OF 1

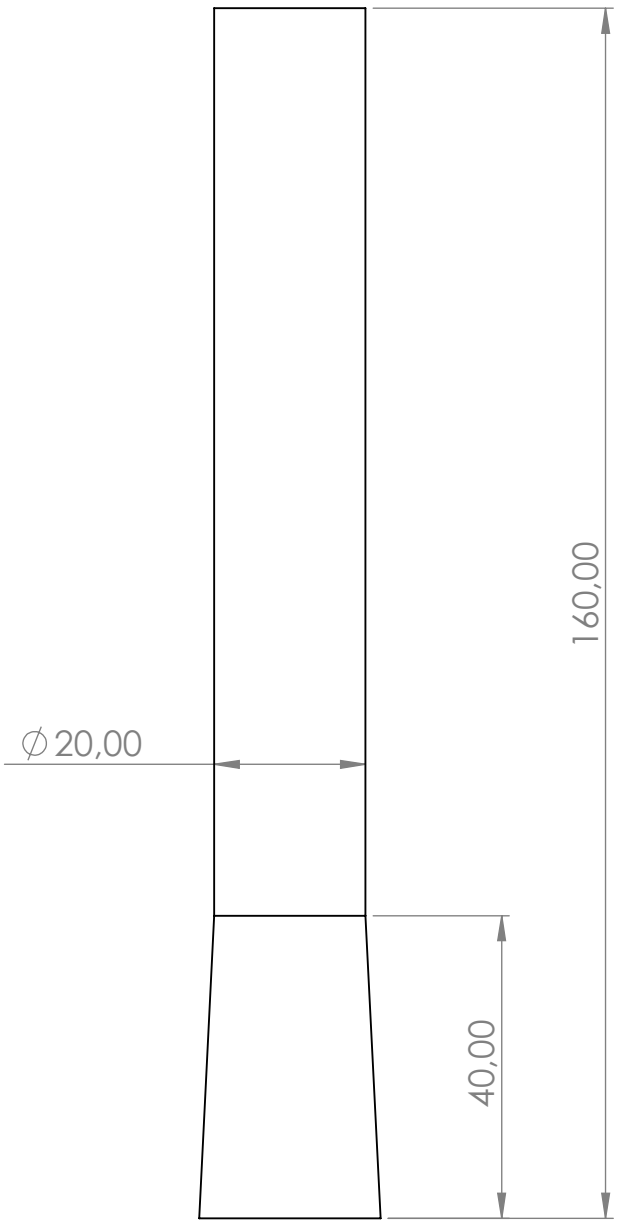

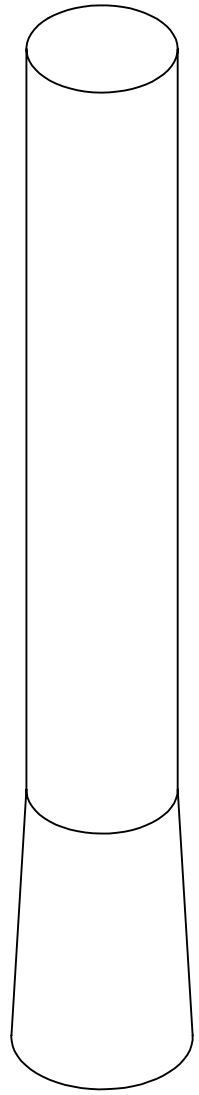

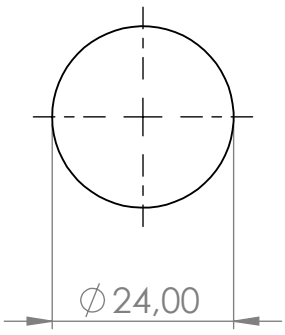

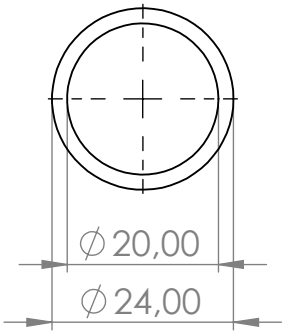

UNLESS OTHERWISE SPECIFIED: DIMENSIONS ARE IN MILLIMETERS SURFACE FINISH: TOLERANCES: LINEAR: ANGULAR:	FINISH:	DEBURR AND BREAK SHARP EDGES	DO NOT SCALE DRAWING / REVISION

	NAME	SIGNATURE	DATE
DRAWN			
CHK'D			
APPV'D			
MFG			
Q.A			

TITLE:

MATERIAL:

DWG NO. Rod

A4

WEIGHT:

SCALE:1:1

SHEET 1 OF 1

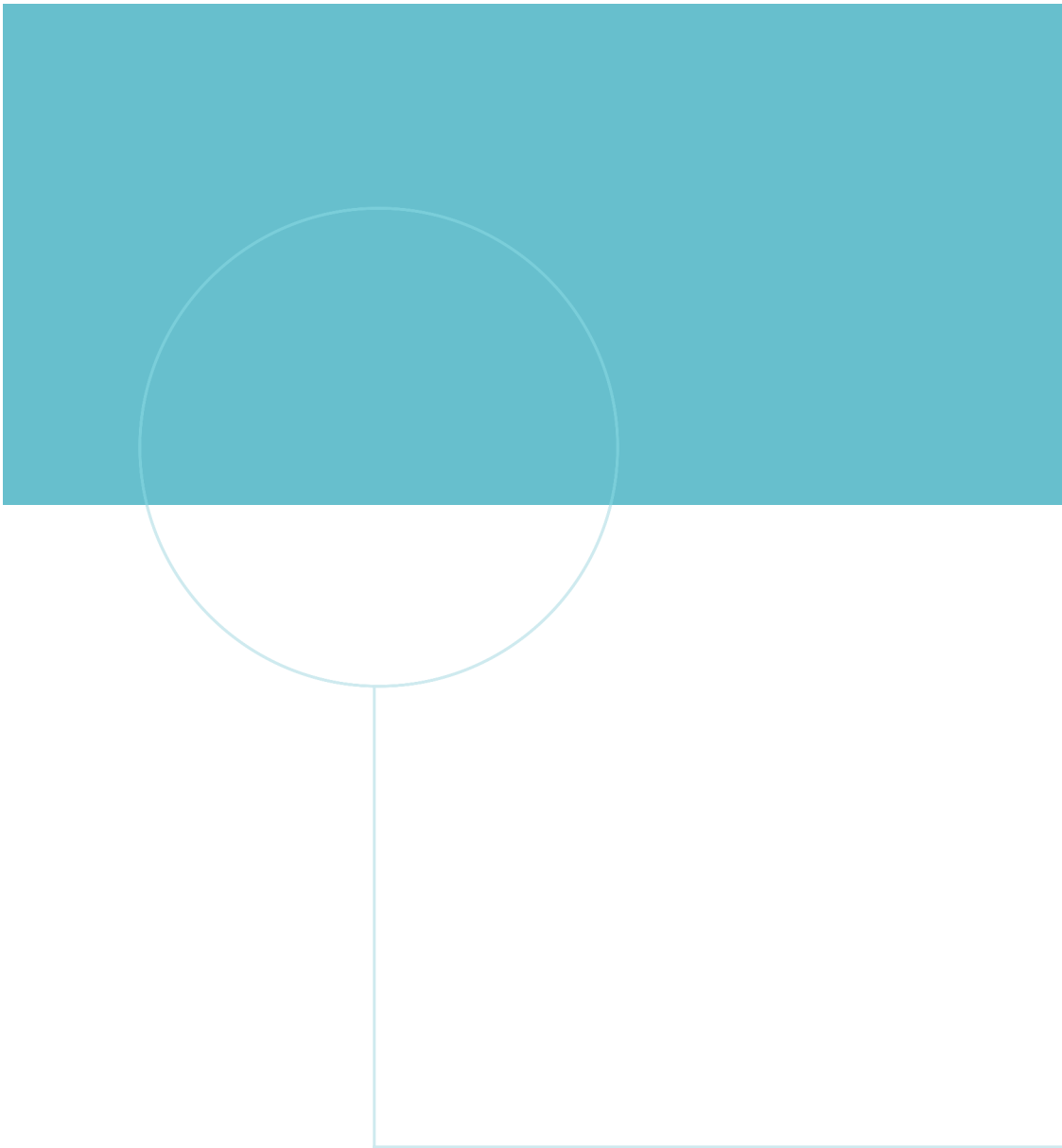

NTNU

Kunnskap for ei betre verd